2013

Brain Landmarks and Paleoneurology: Comparing Physical and Laser Scan Endocasts in Living Hominoids

Ana Pedro

DEPARTAMENTO DE CIÊNCIAS DA VIDA

FACULDADE DE CIÊNCIAS E TECNOLOGIA
UNIVERSIDADE DE COIMBRA

Brain Landmarks and Paleoneurology: Comparing Physical and Laser Scan Endocasts in Living Hominoids

Ana Sofia Pereira Pedro

2013

DEPARTAMENTO DE CIÊNCIAS DA VIDA

FACULDADE DE CIÊNCIAS E TECNOLOGIA
UNIVERSIDADE DE COIMBRA

Brain Landmarks and Paleoneurology: Comparing Physical and Laser Scan Endocasts in Living Hominoids

Dissertation presented to Universidade de Coimbra in fulfillment of the requirements needed to obtain the Master degree in Evolução e Biologia Humanas, accomplished under the scientific supervision of Doctor Emiliano Bruner (CENIEH) and Doctor Eugénia Cunha (Universidade de Coimbra) .

Ana Sofia Pereira Pedro

2013

ACKNOWLEDGEMENTS

I wish to take this opportunity to convey my appreciation for all the people that made it possible for me to accomplish this work.

First I would like to express my gratitude to my supervisors, Doctor Eugénia Cunha and Doctor Emiliano Bruner for guiding me and advising me throughout this study. I am thankful to Professor Eugénia for helping me to choose the theme of this thesis, and for her support and availability. I thank Emiliano for introducing me to the fields of Paleoneurology and geometric morphometrics, and for guiding me along the progression of this work. I am grateful for his interest and enthusiasm which had a positive impact on the way I carried my work, and which lead me to really appreciate these fields of study.

I acknowledge the Centro Nacional de Investigación sobre la Evolución Humana (CENIEH) for receiving me into their facilities and lending the material in which this thesis is based.

It is with great joy that I thank all the people from the CENIEH and Burgos that made my stay easier. I appreciate the time Manny spent showing me how to use the various software required for working with geometric morphometrics and for editing images. I also thank Mario for his availability in helping me and keeping me into knowledge about events and activities. I am grateful to Mario, Isi, Lucia, Marina, David, Cristina, Joseba, Ana, Carlos, and many others, for the warm welcoming, the friendship, the nice “desayunos” and the awesome Friday nights. I wish to note that I am glad I have met all of you guys.

It is also with great happiness that I show my appreciation for the understanding and support of my boyfriend, Bruno. This influenced my moments of loneliness and homesickness for that I had someone I could always lean on.

To my sister Sara, I am grateful for the conversations and shared worries about the challenges and expectations for the future, and nice hints about the writing.

I am thankful to those who visited me in Burgos, for bringing me a little piece of home.

Finally I wish to put into words my deep gratitude to my parents, who allowed me to travel to Burgos for my studies and sustained me the whole time, and without whom I wouldn’t be able to complete this work.

ABSTRACT

Paleoneurology studies brain evolution through the analysis of endocasts (endocranial moulds), that display features of the endocranial tissues, including the brain. Currently, the study of shape relies on the statistical tools provided by geometric morphometrics, which is based on landmark data. Landmarks are anatomical points defined by Cartesian coordinates in 2 or 3 dimensions, which are correspondent between species. The consistency of a study depends upon the repeatability and precision of the landmarks included. The application of landmark data analysis on endocasts is further influenced by the difficulties in identifying cortical brain regions to localize cortical landmarks. These difficulties can increase when dealing with digital casts. This study compares physical and digital endocasts from living hominoids to evaluate the uncertainty associated with the localization of major cortical references, and how this can be influenced by the different data source. Nineteen 3D brain landmarks coordinates were collected ten times from physical endocasts and ten times from their laser scanned surface replicas, from seven species (*Homo sapiens*, *Pan troglodytes*, *Pan paniscus*, *Gorilla gorilla*, *Pongo pygmaeus, Hylobates moloch* and *Symphalangus syndactylus*). Error analyses were computed to assess the reliability of each reference point depending upon the cortical area and the type of endocranial reconstruction (physical or digital). Results suggest that cortical brain landmarks on endocasts show a good reliability and can be used for taxonomic analysis. Although with different patterns of variation, both physical and digital data give similar results. The less reliable landmarks are those located on the parietal bosses.

Keywords: paleoneurology; error assessment; surface scan; geometric morphometrics

RESUMO

A Paleoneurologia estuda a evolução cerebral através da análise de moldes do endocrânio (“endocasts”), os quais exibem estruturas dos tecidos endocranianos, incluindo o cérebro. Actualmente, o estudo da forma baseia-se em ferramentas estatísticas fornecidas pela morfometria geométrica, baseada em pontos de referência (“landmarks”). Estes são pontos anatómicos definidos por coordenadas Cartesianas em 2 ou 3 dimensões, e correspondentes entre espécies. A coerência de um estudo depende da possibilidade de repetição e da precisão destes pontos. A aplicação de uma análise de morfometria geométrica em moldes endocranianos é influenciada pela dificuldade em identificar as regiões cerebrais para localizar pontos de referência do córtex. Estas dificuldades podem aumentar quando se usam moldes digitais. Este estudo compara moldes físicos e digitais de primatas antropomorfos modernos para avaliar a incerteza associada à localização das principais referências corticais, e como esta pode ser influenciada pelo tipo de molde usado. As coordenadas tridimensionais de dezanove pontos de referência foram recolhidas dez vezes dos moldes físicos e dez vezes das suas réplicas digitais. Sete espécies foram analisadas (*Homo sapiens*, *Pan troglodytes*, *Pan paniscus*, *Gorilla gorilla*, *Pongo pygmaeus, Hylobates moloch* and *Symphalangus syndactylus*). Realizaram-se análises de erro para verificar a precisão de cada ponto, dependendo da região cortical e do tipo de reconstrução endocraniana (física ou digital). Os resultados sugerem que os pontos de referência corticais em moldes endocranianos são relativamente fiáveis, podendo ser utilizados em análises taxonómicas. Embora com diferentes padrões de variação, tanto os moldes físicos como os digitais dão resultados semelhantes. Os pontos menos fiáveis foram os localizados nas bossas parietais.

Palavras-Chave: paleoneurologia; análise de erro; scan de superfície; morfometria geométrica

TABLE OF CONTENTS

LIST OF FIGURES

LIST OF TABLES

1. INTRODUCTION

1.1. STUDIES ON BRAIN EVOLUTION

Humans have always been fascinated about themselves. We have spoken and written language, art (like music, painting, poetry, and cinema), we outpace any other great apes on tool use, logical thought and emotional feelings. And we are the only species interested in explaining our abilities. To do so, “we must look to the brain” (Rilling, 2006: 65) to unveil the characteristics that make us different and the mechanisms of evolution that led to our emergence.

1.1.1. Human Brain Anatomy

The central nervous system (CNS) is divided into two main anatomical parts: the brain, which is contained within the cranial cavity and the spinal cord, linking the brain and the rest of the body. The brain is formed by three regions that can be identified during the embryo development: the prosencephalon (forebrain), the mesencephalon (midbrain), and the rhombencephalon (hindbrain) (figure 1.1a) (Seeley *et* al., 2008). The prosencephalon is later divided into telencephalon, which becomes the cerebrum, and diencephalon; and the rhombencephalon divides into metencephalon, becoming pond and cerebellum, and myelencephalon, which becomes the medulla. The medulla, pons and midbrain constitute the brainstem, which makes the connection between the spinal cord, the cerebellum and the remaining brain (Seeley *et* al., 2008). The diencephalon, containing the thalamus and hypothalamus, is located between the brainstem and the telencephalon. The telencephalon or cerebrum constitutes the largest portion of the brain weight (Seeley *et* al., 2008). It is divided into left and right hemispheres by the longitudinal fissure (figure 1.1b). The external layer of the cerebrum is the cerebral cortex (gray matter) which is composed mostly by neuron cell bodies and dendrites, surrounds the white matter, composed of the axons that connect the neurons (Rilling, 2008).

The cerebral cortex is such a large layer in human beings that it displays a series of folds, forming the gyri (ridges) and sulci (depressions) that characterizes our brain (Rilling, 2008). Although the general pattern of the gyri is similar among normal brains, some variation exists between individuals and between the two hemispheres (Seeley *et* al., 2008). The major sulci divide the brain into the four lobes, named after the skull bones overlying each one: frontal, parietal occipital and temporal (figure 1.1b) (Rilling, 2008). The central sulcus extends across the lateral surface and is located about the midway along the length of the brain, between the precentral gyrus and the postcentral gyrus (Seeley *et* al., 2008). It mainly separates the frontal lobe from the parietal lobe (Rilling, 2008). The lateral sulcus or Sylvian fissure delimits the temporal lobe relatively to the rest of the cerebrum (Rilling, 2008; Seeley *et* al., 2008). The occipital lobe is separated from the parietal lobe by the parieto-occipital sulcus or perpendicular sulcus. The brain sulci are fundamental anatomical landmarks, but according to Ribas and colleagues (2006) their localization and visual identification is difficult in a surgical point of view as it commonly varies across individuals. Regarding this, the authors analyzed the neural relationships between important sulcal points and their relationship with cranial points (e.g. bregma, opisthocranion) and demonstrated that cranial and brain landmarks display a reciprocal spatial relationship. They provided evidence that such relationships are relatively constant. Their findings can help understand the tridimensional anatomy and relationship between brain and skull.

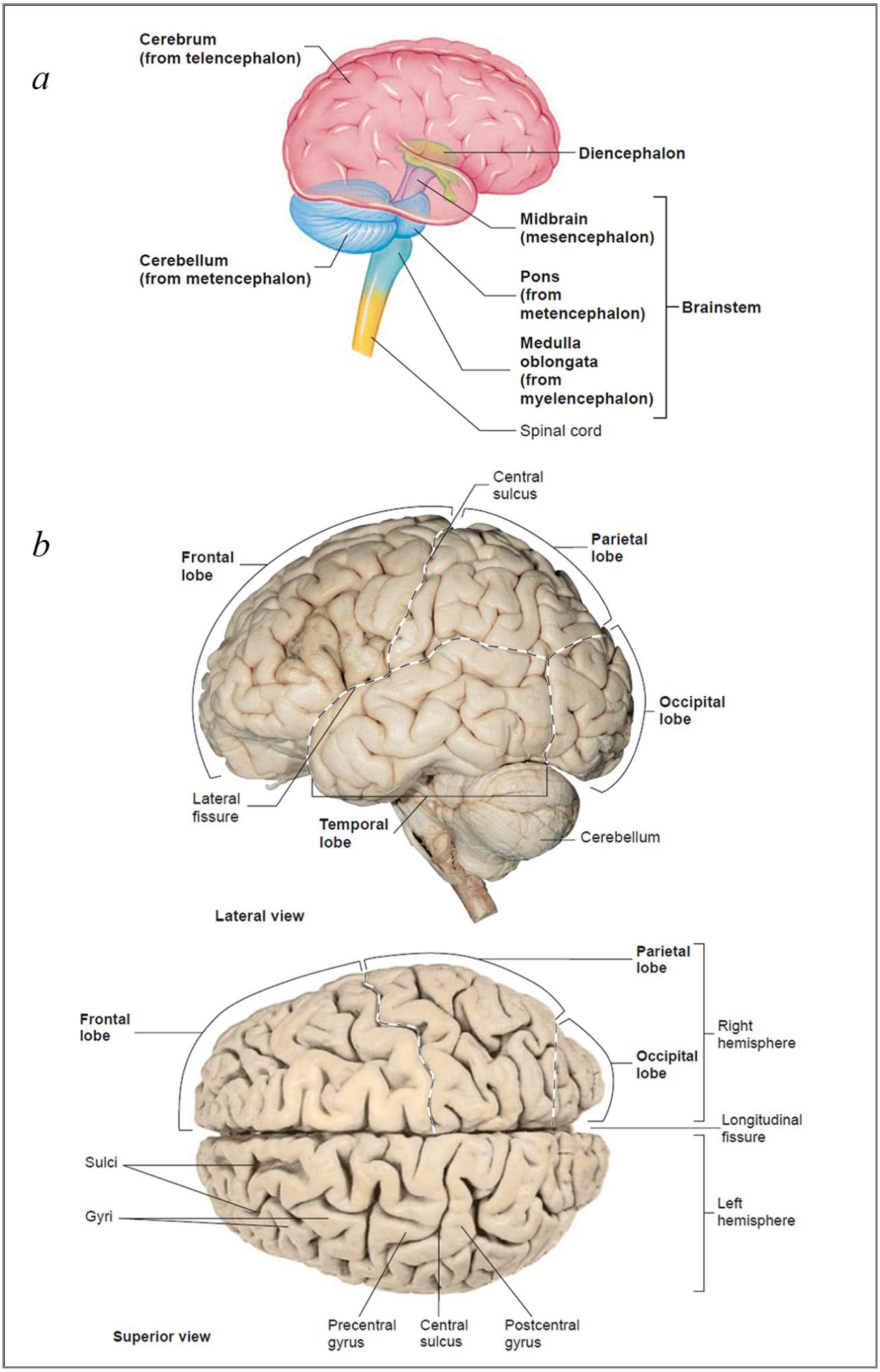

Figure 1.1. Divisions of the adult human brain: developmental regions (a) and the main sulci, gyri and lobes that define the brain. Adapted from Seeley *et* al. (2008).

1.1.2. Functional Craniology

Functional craniology was introduced fifty year ago by Moss and Young (1960). They hypothesized that the morphogenesis of the skull is part of a functional complex of tissues, including the brain and meninges, orbital and oral contents. To exemplify this, the authors mentioned an unpublished experiment in rats: when they increased the rats intracranial volume by adding cerebrospinal fluid, the cerebral capsule and the bones increased and assumed a more globular shape. Conversely, when brain portions were removed, decreasing the volume, the cerebral capsule and bones decreased and turned more flattened. The cranial sutures, as flexible joints allow the skull to change in shape during growth (Di Ieva *et* al., 2013). By studying the effects of premature fusion of one or more cranial sutures (craniosynostosis) on head shape, Richtsmeier and colleagues (2006) proved the association between skull and brain shapes. According to the authors, this association suggests that the brain and skull are interacting with the changing pattern of sutures closure, and, in an evolutionary point of view, a shift in suture closure pattern may be linked to brain and skull shape changes. Size and shape (form) of the skull at a given moment, during ontogeny or evolution, is determined by the functional demands of the soft tissues underneath (Moss and Young, 1960). In other words, the form of the inner surface of the cranial bone is a reflection of the form of the brain (Richtsmeier *et* al., 2006).

Based on these functional and structural relationships, the functional craniology studies the evolution of the human cranium as a system of complex relationships (Bruner, 2007). According to Bruner (2007), the vault, the face and the base of the skull, each influences and is influenced by the brain morphogenesis in its own way. Any little change in one of the components of this network (e.g. intracranial pressure distribution) will imply evolutionary changes in the neurocranial morphology. Therefore, the knowledge of the relationships between the brain and cranial bones during morphogenesis is of great importance for the study of human evolution.

1.1.3. Paleoneurology and Endocasts

As the brains do not fossilize, the study of brain evolution is only possible through the analysis of the fossil endocranial traits (Bruner, 2003). This is the field of Paleoneurology, which examines endocranial casts (endocasts) in order to unveil the external morphology of the brain (Falk, 1987 *in* Bruner, 2003). Used as molds of the brain, the endocasts provide information about its general shape, volume, maybe the convolutions, and imprints of associated structures like blood vessels, cranial nerves and sutures (Holloway *et* al., 2004; Falk, 2012) (figure 1.2). The relationship between the cerebral districts can be assessed as well (Bruner, 2003), giving some clues about the evolution of this organ on extant and extinct hominids.

The endocasts can occur naturally, in a particular taphonomic event, when fine sediments enter the skull through the foramina, filling its inside, and then are compacted and solidified, forming a rock that molds the endocranial surface (Holloway, 1975). When there are no natural endocasts, these can be prepared by applying liquid rubber latex to the endocranial surface through the foramen magnum, building successive layers until reaching a given reasonable thickness (Holloway, 1975). This latex rubber is cured by heat and then collapsed from the skull and the dimensions are stabilized with plaster. More recently, endocasts are also being made using three dimensional imaging techniques (e.g. Schoenemann, 2006).

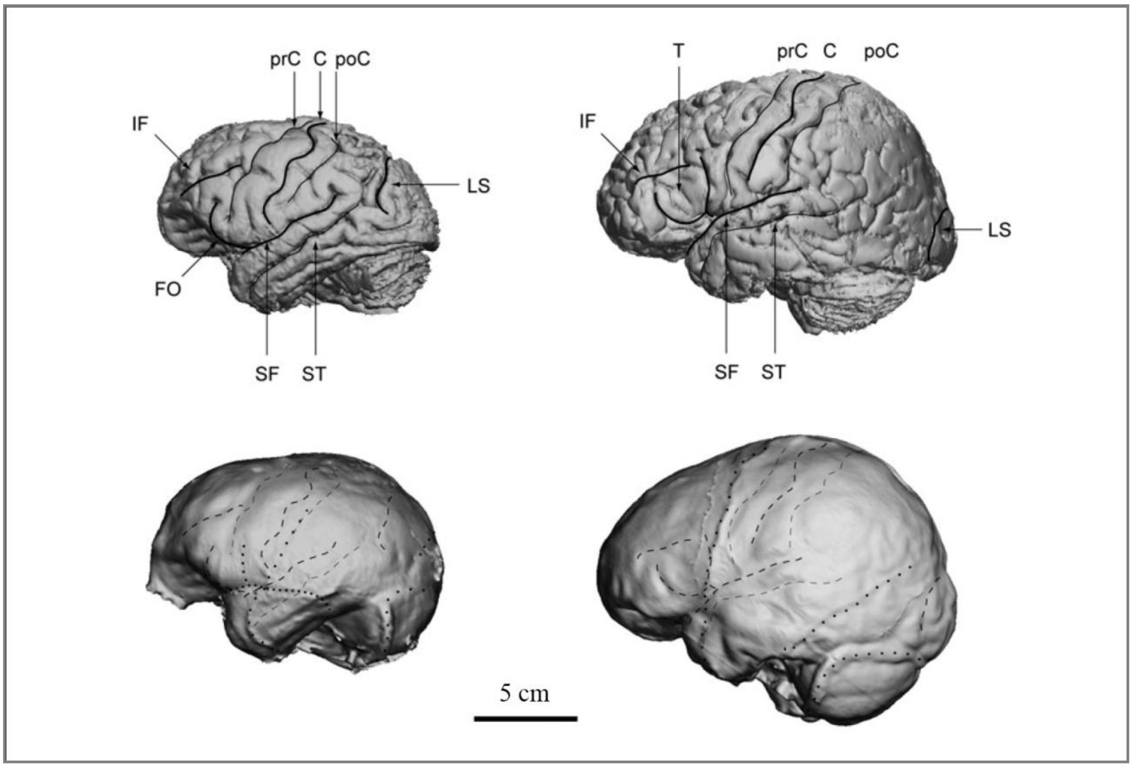

Figure 1.2. Brain and endocast of a chimpanzee (left) and a human (right). Above the brain structures are identified: central, precentral and postcentral sulci (C, prC, poC); fronto-orbital sulcus (FO); inferior frontal sulcus (IF); lunate sulcus (LS); Sylvian fissure (SF); superior temporal sulcus (ST); Pars triangularis, (T). Below the brain structures are delimited on the endocranial surface. (in from Zollikofer and Ponce de Léon, 2013).

However, being natural or constructed physically or digitally, one must draw attention to the fact that endocasts are only models of the endocranial structures and not the original ones, and then any inference about the brain morphology must be cautious (Bruner, 2003). In fact, there are some difficulties regarding the endocasts analysis: the identification of the anatomical references, the definition of boundaries, the dependence on the orientation of the cast, the possibility to touch it, the limitation of the statistical analysis by the small sample and the experience of the observer (Bruner, 2003). Despite these limitations, Paleoneurology is the only direct line of evidence and the main tool to study human brain evolution in fossil species (Holloway *et* al., 2004; Bruner, 2003).

1.1.4. Brain Evolution and Development

During human evolution, as the cranial capacity increases (encephalization), the morphology of the brain had to change in accordance (allometry) (Bruner *et* al., 2003; Bruner, 2004).

Comparison to living hominoids

Humans have the biggest brains among primates, with volumes ranging from around 1100 to 1700cm^3 (Falk, 2007). Great apes display cranial capacities of 275-752cm^3, well separated from that of lesser apes (gibbons and siamangs), whose brain volume values, overlapping with those of monkeys, are about 100 cm^3 (Falk, 2007) (figure 1.3). Encephalization, a larger increase in brain size than in body size during evolution of a lineage, is markedly variable among primates (Boddy *et* al., 2012), and its patterns diverge across mammalian groups (Schultz and Dunbar, 2010). Absolute brain size was shown to be the best predictor of cognitive abilities (Deaner et al., 2007). Among primates, brain size is linked to social learning abilities (Reader and Laland, 2002) and it is linearly correlated with its number of neurons (Gabi *et* al., 2010). In terms of number of cells, the human brain is a scaled up primate brain (Herculano-Houzel, 2012) but they are qualitatively different in terms of morphology (Rilling, 2006).

The different evolutionary processes in the phylogenetic divergence between humans and the other apes resulted in distinct morphological patterns. According to Aldridge (2011), the main morphological changes in brains of human comparing to non-human apes are the anteroposterior and mediolateral expansion of the frontal regions, expansion of temporal lobes and anterior parietal regions, and reduction of occipital poles, both cortically and subcortically. Furthermore, each ape differs from human patterns in a specific way. Regarding the endocranial shape, Bienvenu and colleagues (2011) confirmed globularity and basicranial flexion to be typical of humans. This characteristic had been determined before by Lieberman and coworkers (2002). The non-human African apes are characterized by more elongated endocranial shapes with the gorillas displaying the longer, narrower and less flexed cranium; and orangutans have short braincases with wider space between frontal poles (Bienvenu *et* al., 2011).

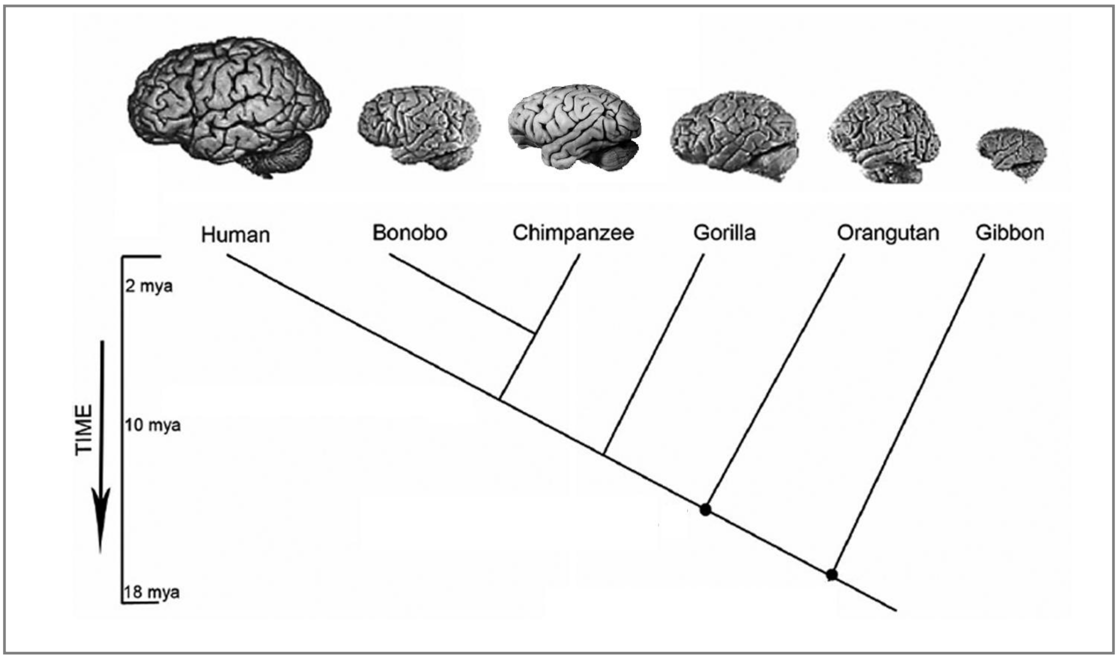

Figure 1.3. Cladograms showing the lateral views of extant hominoids brains and the evolutionary divergence between them. Adapted from Semendeferi *et* al. (2011).

Hominid brain evolution

Among the fossil hominids, brain size has been increasing throughout evolution (figure 1.4). Endocranial volumes of Australopithecines range from 387 to 560 cm^3, with those of *Homo erectus sensu lato* being relatively larger, (727 - 1390 cm^3), and the *Homo neanderthalensis* displaying higher volumes (1200 - 1740 cm^3) [based on Appendix 1 from Holloway *et* al., (2004)]. Australopithecines brain sizes overlap with those of great apes and the Neanderthals volumes overlap with those of modern humans, with the *H. erectus/ergaster* values lying in between.

Australopithecus have brain shapes lying between those of chimpanzee (more elongated) and modern humans (more globular) (Neubauer *et* al., 2012), with a reduction of primary visual cortex and a relative increase of the posterior parietal cortex (Holloway et al., 2004). From Australopithecines to *Homo erectus* brains became wider relatively to length and undergone a reorganization of the frontal lobe

(Bruner and Holloway, 2010). Further changes in shape with increasing encephalization occur within the genus *Homo*. According to Bruner (2004), in comparison to *Homo erectus/ergaster*, Neanderthals and modern humans have brains that are vertically enlarged. Frontal areas, flat and narrow in archaic *Homo*, developed in width on Broca's cap, relatively to the maximum width (parieto-temporal); in height, with elevation of the vault; and in length, as the lateral sulcus shifted to a more posterior position (Bruner, 2004). Parietal areas became wider and higher as well, but shortened, while the occipital areas developed vertically but reduced in length and width (Bruner *et* al., 2003; Bruner, 2004). Between *Homo erectus s. l.* and Neanderthals the endocranial differences in shape are basically related to the increasing in size, whilst modern humans, although having similar allometric pattern, display a separate evolutionary trajectory related to the parietal development (Bruner *et* al., 2003). Although the parietal areas enlarged on both Neanderthals and modern humans (Bruner, 2008), the former have short and flattened parietal lobes and in the latter the enlargement of the structure is more uniform, with differences more pronounced in the upper parietal areas (Bruner, 2004, 2010). Consequently, there is an approaching between the temporo-cerebellar and frontal areas, leading to the more globular morphology of the modern human brains (Bruner *et* al., 2003; Bruner, 2004). Thus, according to Bruner *et* al., (2003), modern humans and Neanderthals reached similar brain sizes following independent evolutionary trajectories, resulting in different morphologies. The authors hypothesized the parietal development of *Homo sapiens* can be a bypass to overcome the biomechanical stress caused by encephalization, namely the "ontogenic stress" (Di Ieva *et* al., 2013) causing the cranial hyperostotic characters displayed by Neanderthals.

Brain changes during development

The adult brain morphology is a result of the changes in shape and size during ontogeny. Based on endocranial morphology, Neubauer and colleagues (2009) studied the human brain ontogenic shape and size changes. In relation to shape changes, the human endocranial morphogenesis can be divided into three distinct phases: the perinatal, from birth to 1 year of age; the childhood, until 9 years; and the adolescent phase, until adulthood (Neubauer *et* al., 2009). Each phase is characterized by different trajectories of shape change: on the perinatal phase there is a parietal bossing and an overall midline basicanial flexion, which shifts to a basicranial angulation during the childhood phase, and on the adolescent phase the shape alterations are more localized, on the orbital and frontal areas (Neubauer *et* al., 2009). According to the authors these bends in shape change trajectory don't correspond to the transition from high to low growth rates, i.e. to size changes. This and the fact that the brain shape continues to change after the adult size has been achieved, reinforce the idea that the shape changes aren't only influenced by size increase (Neubauer *et* al., 2009).

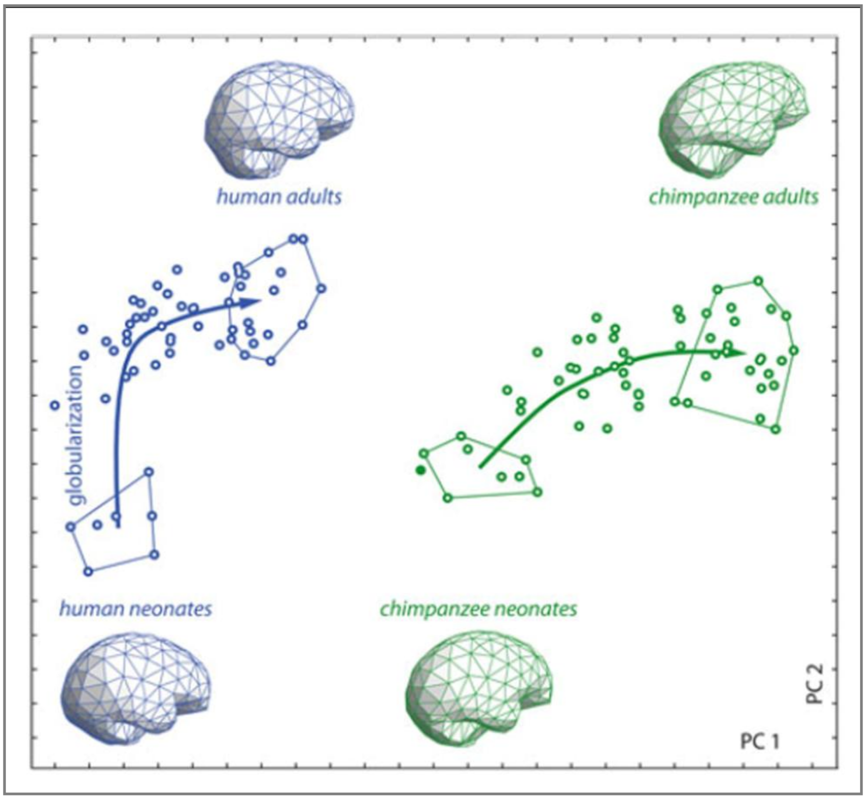

Figure 1.4. Endocranial shape changes during development after birth in human and chimpanzee. The trajectories indicate the shape changes from neonates to adults, with the mean shapes of witch shown as wireframes (Neubauer and Hublin, 2012).

Comparing to humans, the chimpanzees have similar patterns of endocranial development but different trajectories. Neubauer and colleagues (2010) performed developmental simulations, applying the other species trajectory to neonates and to specimens with incomplete deciduous dentition (age group 2), and found out that when using the neonates, the simulated adult morphology would resemble the real adult, but not when using the age group 2. They report that some shape differences between the two species are already established at birth and humans have a different perinatal phase of shape changes before they enter the common pattern with the chimpanzee, the "globularization phase". But not only chimpanzees lack the globularization phase, Neanderthals do as well (Gunz *et* al., 2010).

The uniquely human pattern of brain morphology is the basis of the uniquely human cognitive characteristics (Bruner, 2004; Neubauer and Hublin, 2012) and may explain the brain disorders observed only in humans (Aldridge, 2010; Neubauer and Hublin, 2012; Bruner and Jacobs, 2013)

1.2. ANTHOPOLOGY AND MORPHOMETRICS

1.2.1. Digital Anthropology

The current advances in neurosciences are the background for modern paleoneurological studies (Bruner, 2007), providing techniques that can help to understand the biological organization behind the brain form (Rilling, 2008). According to Zollikofer and colleagues (1998:41), computer-assisted paleoanthropology "complements classical methods of physical anthropology with a set of novel tools in three major areas: visualization of hidden anatomical features, morphometric and biomechanical analysis of skeletal structures, and computer-assisted reconstruction of fragmentary fossils." Computed tomography (CT) is an imaging technique consisting on a source of X-rays and a correspondent detectors array that rotate around an object (Bruner and Manzi, 2006).It produces attenuation data from different angles that can be integrated to generate digital cross-sectional images which are shown on a computer monitor, in a scale of grey, with the lowest density structures represented in black and the highest density ones in white (Spoor *et* al., 2000). As the CT images obtained are composed by pixels (picture elements), each pixel representing the specimen density at one location, it is possible to isolate specific anatomical regions, for instance extracting the labyrinthine cavities from the temporal bone (Zollikofer *et* al., 1998). The size of the pixel relatively to the field of view (FOV) and mainly the geometry of the X-ray beam will determine the resolution of the resulting image, which is usually in the range of 0.3 - 0.5 mm (Spoor *et* al., 2000). For smaller structures, like dental enamel, micro-CT scans can be used, scanning at resolutions below 0.1 mm (Zollikofer *et* al., 1998).

Rilling (2008) mentions other imaging methods that are used complementary to CT with different purposes, as they access the hidden structures. He divides these methods into structural, including magnetic resonance imaging (MRI) and diffusion tensor imaging (DTI), and functional, registering brain activity, like positron emission tomography (PET) and functional magnetic resonance imaging (fMRI).

The outer shell of an object can be accessed using surface scanning, a new method overviewed by Friess (2012). This method is based on non-ionizing radiation, i.e. visible light. The differences between the surface scanner models are related to the light source (laser or structured light), FOV, resolution, and the measurement principle (e.g. time-of-flight (TOF) and triangulation based scanners). According to the author the surface scanning process comprises the oversampling of the specimen through multiple views, then processing the acquired images by aligning the views, eliminating redundant points and fusing into a cloud object. The post processing includes noise reduction filtering, which can be performed repeatedly during the scanning process, and gap filling, an optional step that is more efficient performed as last step. The author lists some advantages of the surface scanning: the non-destructive and non-invasive character of the measurements, the shorter post-processing steps, the high resolution, the possibility of capturing texture of the specimen’s surface, the affordability and high degree of mobility, and the utility to morphometric studies. The choice of the device depends on the performance of the scanners, which is based various parameters: the FOV determines the size of the specimen; the resolution, which is the number of the pixels per millimeter of the FOV; the accuracy and precision which determines the error; the acquisition speed, avoiding noise from movement of living specimens; portability, which can affect accuracy and precision; and cost, depending on the quality of the optics and software.

The digital methods bring many advantages to the study of fossils and human evolution. They are noninvasive techniques which allow obtaining detailed information, in 2 or 3 dimensions, about the exterior and interior structures of the specimen in analysis (Zollikofer *et* al., 1998). Plus, the digital 3D structure of the fossils can be virtually reconstructed and manipulated by the users, what prevents the invasive handling of the real fossil. Gunz and colleagues (2009) established some principles to virtually correct deformed fossils or reconstruct missing parts. As the deformed or incomplete pieces are difficult to articulate and can be aligned in more than one way, the reconstruction must be based on morphological and anatomical expertise. They described two methods for fossil reconstructions by combining digital data with geometric morphometrics tools (figure 1.5). The deformed and missing structures can be assessed based on deviation from symmetry, which can be restored, if the midline is intact and only one side is distorted or the deformation is uniform, by mirror the image. When these conditions are not verified the assessment of the missing points can be predicted using information from other complete fossils. The reference fossils used largely influences the resulting reconstruction, and, in the absence of a group of specimens to which the deformed fossil belongs the choice of the reference specimen must be cautious and depends on the purpose of the reconstruction.

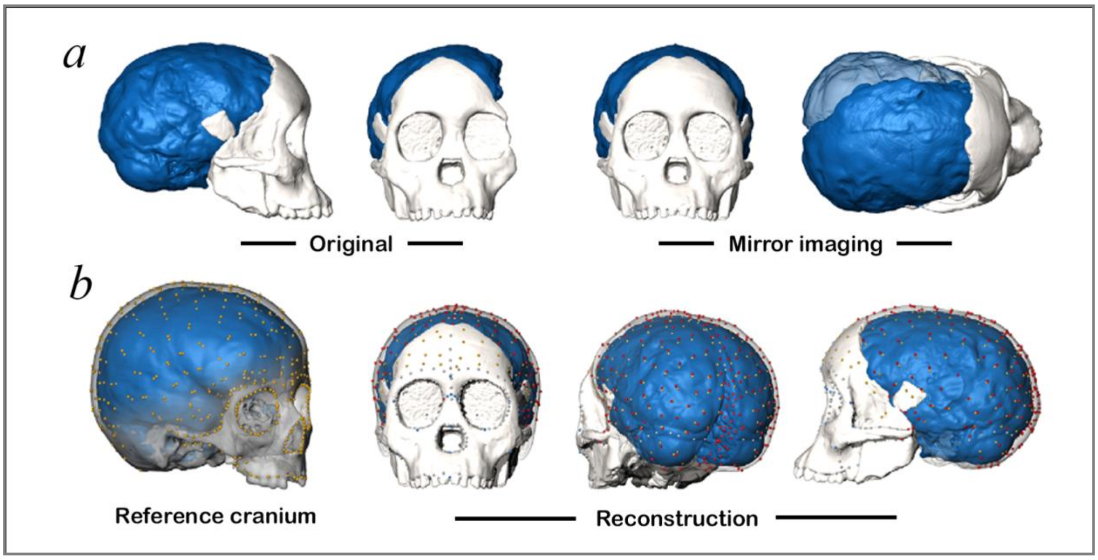

Figure 1.5. Reconstruction of the Taung endocast by (a) mirroring the image and by (b) using a reference cranium (a modern human child) (Gunz *et* al., 2009).

Various authors (Zollikofer *et* al., 1998; Bruner and Manzi, 2006) defend the creation of a digital data base of virtual fossils, which would constitute an international network providing means for fossil study, preservation and reconstruction. According to Zollikofer *et* al. (1998) the virtual fossils can be converted again into physical copies through stereolithography, which is a noninvasive technique, better alternative to latex or silicon molds, as there is no loss of quality resulting from repeated copying cycles.

1.2.2. Geometric Morphometrics and Landmarking

The analysis of shape has long been an essential part of studies in biology, anthropology and paleoanthropology (Slice, 2007). The early morphometrics where based on measurements of distances directly on the specimen (Rohlf, 1990) but these traditional methods consist essentially of measurements of size, expressing no information about their geometric structure, and cannot be compared anatomically between species (Zelditch *et* al., 2004). The advances in computational tools brought a more sophisticated and objective methodology to analyze shape variation, the Geometric morphometrics (GM) (Adams *et* al., 2004). Geometric morphometrics concerns the study of shape variation and covariation through multivariate statistical analysis of the anatomical landmarks defined by Cartesian coordinates (Bookstein, 1991). These methods present new advantages, like the preservation of the geometric information of the landmarks (Slice, 2007) and the possibility to graphically visualize and easily understand the shape differences (Klingenberg, 2013).

According to Bookstein (1997), the landmark data is the basis of GM analysis. Landmarks are discrete anatomical points which position is recorded by Cartesian coordinates in 2- or 3- dimensions, (Slice, 2007). They should be homologous anatomical loci (i.e. recognized as the same point on different species) (O’Higgins, 2000) that can be located repeatedly and reliably, providing an adequate coverage of the morphology of the specimen (Zelditch *et* al., 2004). The anatomical landmarks are not equally identified on a specimen. Bookstein (1991) devided the landmarks into three types, based on the difficulty to define them: the Type I landmarks are at the intersection of three structures, for instance, the frontal and the two parietal bones meet point is Bregma; the Type II, like Basion, are defined by the geometry of the surrounding anatomy, the curvature of the foramen magnum; Type III are extreme points, like Glabella, which position is defined by distant anatomical structures. The homology is strongest in Type I landmarks. But there are regions of important morphological information that are poor in landmarks, as the neurocranium, so a series of ordered points are positioned along curves or surfaces to quantify the homologous regions: the semilandmarks (Bookstein, 1991). As their initial spacing is arbitrary, the semilandmarks are allowed to slide, maximizing its correspondence across a sample (Gunz *et* al., 2009; Baab *et* al., 2012).

The landmark coordinates are recorded relatively to the (x, y, z) axes, so their values reflect the geometric information of the specimen with respect to those axes (Slice, 2007). In geometric morphometrics, shape is the remaining geometric information after removing variation in scale, location and orientation of an object (Kendall, 1977 *in* Zelditch *et* al., 2004). Thus, the shape of an object is defined by configurations of landmarks that consist of sets of point coordinates. To compare the landmark configurations, the shape information must be extracted from the coordinates, which is performed by the general Procrustes analysis (GPA) (Zelditch *et* al., 2004). The Procrustes superimposition minimizes the differences between landmark configurations by translation, scaling and rotation (figure 1.6a). First, the original landmarks configurations are scaled to the same Centroid Size, which is calculated as the square root of the sum of the squared distances of the landmarks to the centre of the form (centroid) (figure 1.6b) (Slide, 2007). Then the configurations are moved to the same location by superimposing their centroids. Finally they are rotated about the centroid to get into an optimal orientation in which the square distance between the corresponding landmarks is minimal (Klingenberg, 2010). GPA calculates the average shape that is used as reference to optimal alignment, which minimizes the average distances of shapes from the reference (Zelditch *et* al., 2004). When the data include semilandmarks, two GPA are performed, with the sliding step between them (Baab *et* al., 2012).

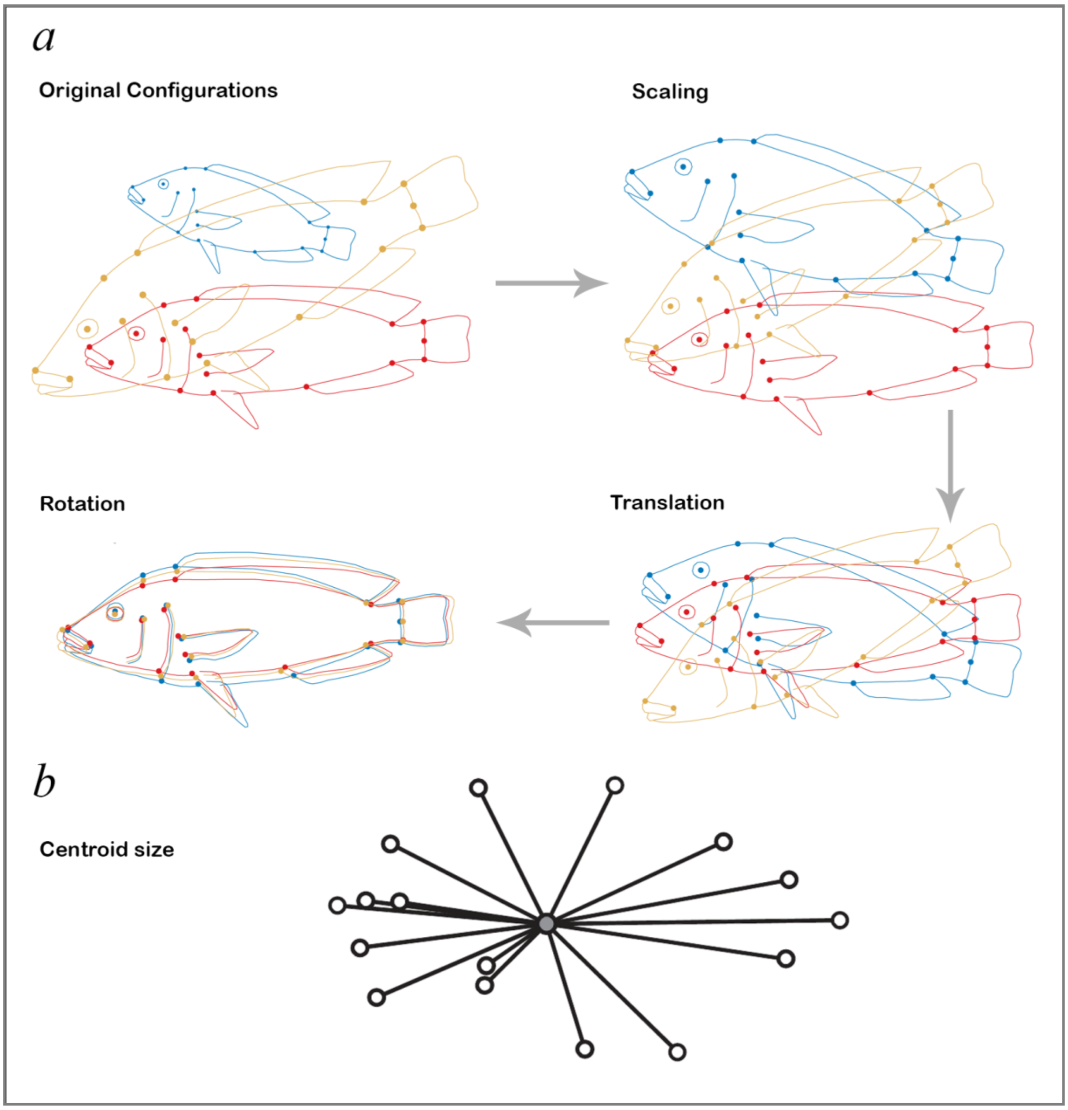

Figure 1.6. Procrustes superimposition: (a) illustrates the various steps to remove shape information from the landmark data (Klingenberg, 2010) and (b) represents the computation of the Centroid size, in which the centroid is the grey dot, connected by the lines to the landmarks (white dots) (Zelditch *et* al., 2004).

After the Procrustes superimposition, the distance between the corresponding landmarks is the variation in shape, which can be characterized in shape spaces (Klingenberg, 2010). The Procrustes distance is a measure of differences in shape in a multidimensional shape space, where similar shapes, represented by points, are closer together, and dissimilar ones are far apart (Rohlf, 1998). According to Zelditch *et* al. (2004) there are three shape spaces: the Kendall´s shape space, which is the space of all possible superimpositions of two specimens; the GPA space, resulting from superimposition of more than two specimens; and tangent space, the Euclidean space, tangent to the GPA space. The tangent space is the space in which the statistical methods can be applied, and the projection of the coordinates into this space is equivalent to the mapping of the earth into a 2D surface (Baab *et* al., 2012).

As the shape variables inherit the complex patterns of variation and covariation of the morphological and functional features of the organisms, the information must be simplified, which is accomplished by the Principal Components Analysis (PCA) (Zelditch *et* al., 2004). This method produces new sets of variables by identifying the orthogonal linear combinations of the original variables that better reproduce the sample variability (Slice, 2007). These new sets of variables, the Principal Components (PCs), are reduced in numbers and simplify the description of variation among individuals in a sample, as the individuals are scored and ordered along the PCs, and the patterns of variation can be visualized on a plot (Zelditch *et* al., 2004). Other methods to simplify the visualization of changes in shape are available. In fact, the visualization tools are considered among the scholars to be one of the great advantages in GM analysis. Klingenberg (2013) makes a resume of the various types of tools that allow the visualization of shape changes. The landmarks displacement or transformation can be seen by using three methods (figure 1.7). The "lollipop" diagrams show the shift in landmarks position through lines that part from the initial shape, indicated by the dots. The wireframe graphs connect the landmarks with lines, and the starting and target shapes are superimposed for comparison. The latter are easier to read as they contain information that can help relating the changes in landmarks locations to the underlying anatomical structures (Klingenberg, 2013). The Thin-plate Splines (TPS) is a tool that allows the representation of shape differences by deforming one shape into the other in a transformation grid (Bookstein, 1991). But the resulting shape changes visualized by either method cannot be interpreted literally as they are determined by the set of landmarks in analysis (Slice, 2007; Klingenberg, 2013).

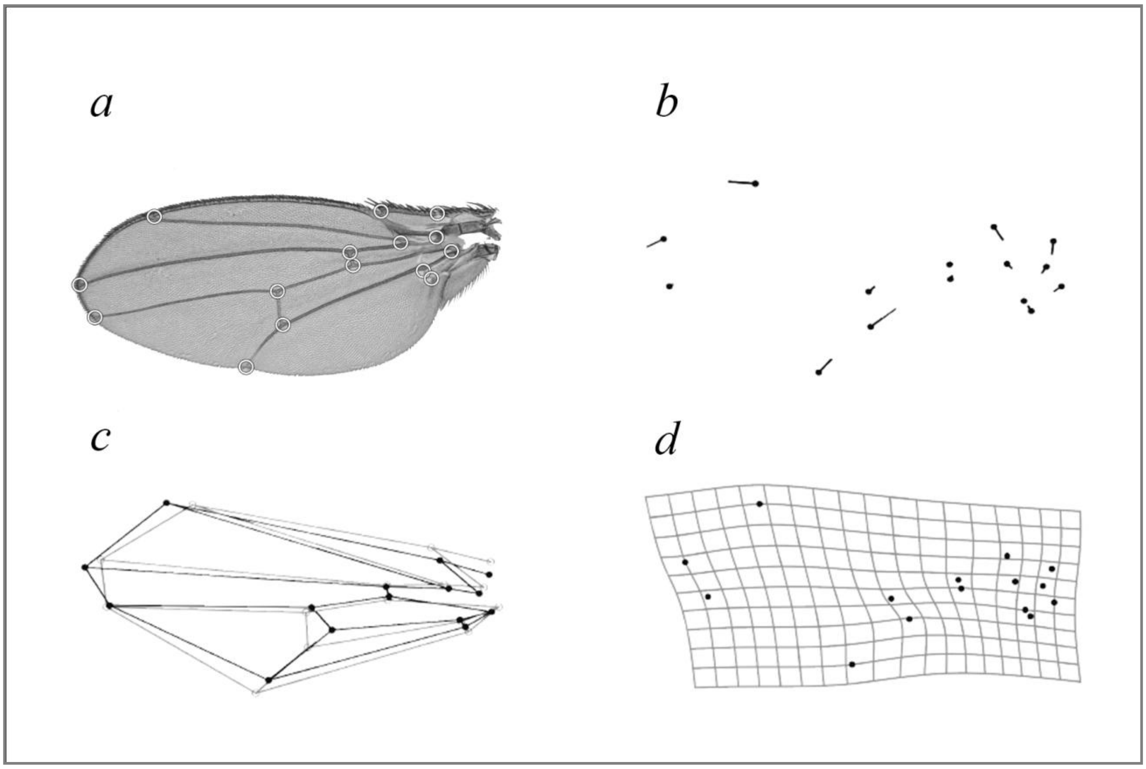

Figure 1.7. Visualization tools in geometric morphometrics for the set of landmarks in a fly wing (a). The methods of landmark displacement are represented in (b) lollipop diagram and in (c) wireframe graph, and the transformation grid is shown in (d) (from Klingenberg, 2013).

The GM methods had been applied to a great number of disciplines in biology and anthropology, like systematics, ontogeny, modularity, genetics (Baab *et* al., 2012), developmental biology (Klingenberg, 2010), and, as seen before, fossil reconstruction (Gunz *et* al., 2009).

Issues and Bias of the landmark data

Despite all of the advantages these new computed and mathematical techniques bring to the study of human evolution, they do not come free of error. As the GM methodologies are based on the landmark data, the set of landmarks used will influence the results (Free *et* al., 2001; Gunz *et* al., 2009). According to Free and colleagues (2001: 811) "if the number of landmarks does not adequately cover the structure of interest then only a partial description of the shape changes is possible." The landmarks identification is also an issue, as there are different types of landmarks with different identification precision in the same study (Cramon-Taubadel *et* al., 2007). Furthermore, the lack of a common coordinate system between the various landmark configurations within a study can cause complex repercussions when trying to interpret the shape differences between them (Richtsmeier *et* al., 2002).

Pinocchio effect

Procrustes superimposition reduces the variation between corresponding landmarks by minimizing their distances. This can be extrapolated to the error associated in locating each landmark: GPA minimizes the overall error by reducing the error of imprecise landmarks and increasing it around the precise ones (Cramon-Taubadel *et* al., 2007). The term “Pinocchio effect” is used to refer to this situation when there is localized variation on a small region of the landmark configuration, metaphorically resembling the tip of Pinocchio’s nose variation relatively to the head (Klingenberg, 2013). But when analyzing differences between landmark configurations one might ask if it is the “tip of the nose” that moves forward or the rest of the head landmarks that move backwards, i.e. which landmarks are responsible for shape changes (Klingenberg, 2013). Both descriptions fail to recognize that the shape change is located between the landmarks, and thus the attribution of shape changes to particular landmarks should be avoided.

This bias inherent to Procrustes superimposition can only be avoided if the specimen remains static and is not moved between sessions of landmark coordinates collection, which are made in a constant frame of reference, i.e. the same coordinate system (Cramon-Taubadel *et* al., 2007), as the main problem is in orientation (Rictsmeier *et* al., 2002). According to Rictsmeier and colleagues (2002), other landmark methods exist that don’t include the superimposition of shapes, as they are based on linear distances connecting pairs of landmarks. One of these methods is the Euclidean distance matrix analysis (EDMA) which measures all possible lengths between landmarks generating a matrix that compares the lengths between corresponding landmarks on different specimens. Within this method the shape does not change with location or orientation but it lacks the advantageous visualization graphs available from GM analysis.

1.3. AIMS OF THE STUDY

The present study is focused on the issues concerning the study of endocasts and the difficulty in locating landmarks, which can induce measurement error. The difficulties regarding the analysis of endocasts are related to the anatomical regions that can be identified. As molds of the endocranium, endocasts display features of brain, cranial and other intracranial tissues, which can difficult the identification of anatomical brain regions and boundaries (Bruner, 2003). Moreover, the identification of brain structures is complicated when the preservation and detail of these structures is poor. The anatomical expertise of the observer is obviously of great importance in identifying regions of interest on the endocasts. Another source of variation is introduced by the object where the landmarks are being collected, i.e. physical or digital specimens (Schoenemann *et* al., 2007; Friess, 2012). When working with digital endocasts further complications are added, as the perception of the anatomical element depends on the perspective of the view. The impossibility of handle the object and the dependence on the orientation of the image makes it more difficult to place landmarks on surface scan endocasts (Bruner, 2003). The incorrect identification of the anatomical structures further complicates the location of landmarks on those regions (Free *et* al., 2001). The different types of landmarks have different precision and reliability in being placed. The equipment precision and accuracy (Friess, 2012) and the observer error (Cramon-Taubadel *et* al., 2007) have to be considered as well.

Therefore, this work investigates the reliability of cortical landmarks on both physical and laser scanned endocasts of extant hominoids. The main scopes are to evaluate the uncertainty associated with the location of major cortical references on endocasts and to assess the differences in using different kind of data (physical and laser scan endocasts). Considering that the present study uses methods for analysis of morphology, the shape differences among the extant hominoids are also explored.

2. MATERIALS AND METHODS

2.1. SAMPLE

The sample is composed of eight endocasts from extant hominoids, available at the Centro Nacional de Investigación sobre la Evolución Humana (CENIEH) All endocasts were made from adult specimens belonging to seven species of apes. Table I shows the specificities of each cast. The physical casts had been obtained from Bone Clones Inc., a company for osteological reproductions, and each has a code (www.boneclones.com) (see Table I). The digital casts used are the 3D images resulting from the laser scanning (NextEngine Inc; resolution: 0.13 mm) of the physical ones, previously constructed by José Manuel de la Cuétara.

Table I- Endocast specimens. The code is the one attributed by Bone Clones Inc. The ID is the one used throughout the present work to refer the endocasts, in the presented sequence.

Code	Endocast	Species	ID
KO-227	Male Bonobo	*Pan paniscus*	**BON**
KO-292-E	Male Chimp	*Pan troglodytes*	**CHIM**
KO-231	Female Chimp	*Pan troglodytes*	**CHIF**
KO-228	Male Gibbon	*Hylobates moloch*	**GIB**
KO-229	Male Gorilla	*Gorilla gorilla*	**GOR**
KO-092-E	Male Human	*Homo sapiens*	**HUM**
KO-232	Male Orangutan	*Pongo pygmaeus*	**ORG**
KO-230	Male Siamang	*Symphalangus syndactylus*	**SIA**

2.2. PROCEDURE

2.2.1. Selection of landmarks

A set of nineteen cortical landmarks were collected from each physical and digital endocast. Eight of the landmarks are bilateral and located symmetrically on left and right sides of the endocasts, making a total of 16 landmarks. The other 3 landmarks are located on the sagittal plane (table II; figure 1). As all the landmarks are located based on maximum curvatures and they are not defined by any anatomical well delimited lines, they can all be considered type III landmarks.

Table II - Description of the cortical landmarks used in the analysis.

	Landmark	Acronym	Description
Bilateral	Frontal Poles	**FP**	Anteriormost point, following maximum length
	Occipital Poles	**OP**	Posteriormost point, following maximum length
	Temporal Poles	**TP**	Tip point
	Cerebellar Poles	**CP**	Lowermost point
	Broca's Cap	**BC**	Maximum curvature point
	Lateral Sulcus	**LS**	Posterior Limit
	Supramarginal Gyrus	**SG**	Maximum curvature point
	Angular Gyrus	**AG**	Maximum curvature point
Sagittal	Central Sulcus	**CS**	Intersection with Interhemispheric fissure
	Perpendicular Sulcus	**PS**	Parieto-occipital boundary
	Internal Occipital Protuberance	**IOP**	Intehemispheric and cerebro-cerebellar separation

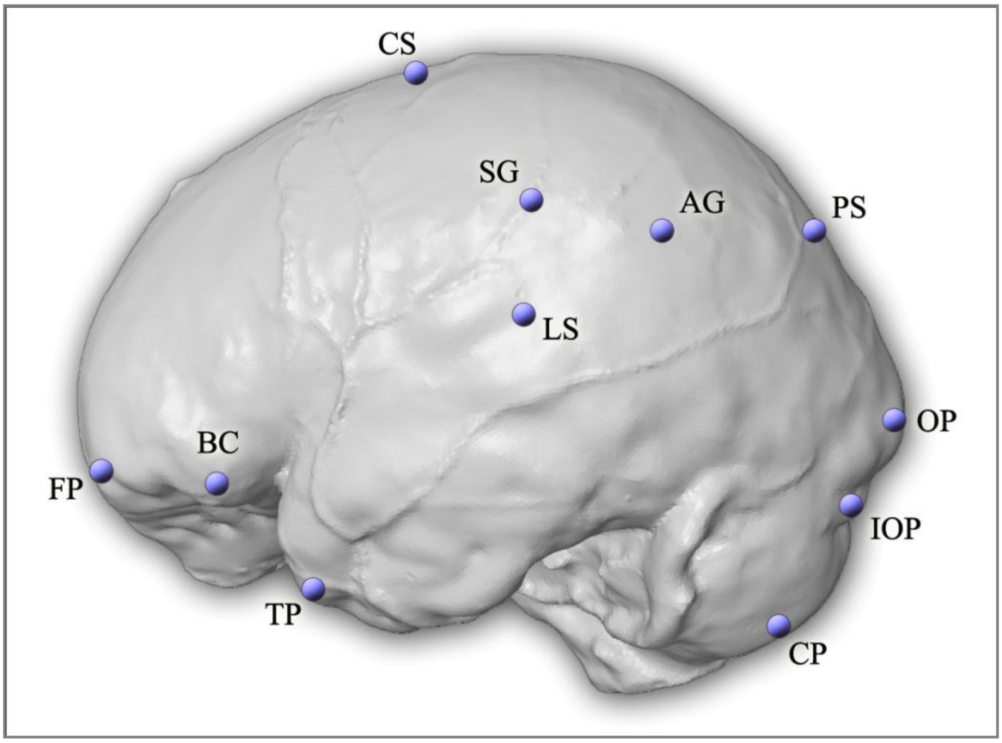

Figure 2.1. Location of the cortical landmarks, on the human endocast, lateral view. See table II for the meaning of the acronyms.

2.2.2. Sampling

Each specimen was sampled ten times (10 times the physical replica and 10 times the digital replica). The sampling sessions took place during two weeks (10 days), and the 19 landmark coordinates were collected two times a day. Physical endocasts were sampled by the morning and the digital ones at the afternoon.

The specimens were sampled in a random order. This way systematic errors caused by improvement of measuring skills through time, or fatigue induced quality deterioration (Hammer and Harper, 2006), as well as memory placement of the landmarks (Valeri *et* al., 1998) can be minimized.

Physical endocasts

For the physical casts, the landmark coordinates (x, y, z) were collected with a Microscribe G2X digitizer (Immersion Corporation: resolution: 0.23 mm). At each sampling session the specimens were fixed in place, using plasticine to prevent movement, and sampled one at a time. Although the effort to position the endocasts with the same approximate orientation, the constant replace of specimens during the sampling session impedes a consistent orientation of a single endocast. Microscribe was connected to a computer and the landmarks 3D coordinates were written directly to text files.

Digital endocasts

The landmark coordinates collection from the digital scans was performed using Landmark Editor (Wiley *et* al. 2005). This software allows the visualization of a 3D image of each endocast that can be rotated to any view, as well as the placement of landmarks on any of these views. On each sampling session the landmarks configuration was placed on every scan endocast, one at a time. The 3D coordinates of each specimen were written to text files and saved individually.

At the end of the sampling all the data from each session, twenty groups of the 19 landmark coordinates (10 physical and 10 digital), were added to a single text file for each endocasts. Then, the data from each endocasts was added to a single text file by the order showed on Table I. This file with 160 groups of landmark coordinates was the one used in the analysis.

2.3. ANALYSIS

2.3.1. Analysis of Error and Variation

The variation at each landmark (discrepancy) was computed by calculating the standard deviation for each landmark coordinate (x, y, z), and then the mean of these values for each landmark point (the mean standard deviation, MSD). A first analysis was computed on the raw values of the digital replicas to assess the absolute error. A second analysis was computed on the whole sample to compare the physical and digital data after being Procrustes superimposed together. The statistical analysis was performed on PAST (Hammer *et* al., 2001).

Absolute Error

To assess the precision in locating landmarks within an endocasts its orientation must be consistent for all the sessions because the location of a given landmark changes with the exact orientation of the endocast (Valeri *et* al., 1998). That way one cannot use the data from the physical endocasts as the distance between the same landmark on data from two different sampling sessions of a given endocast is influenced its orientation. By using Landmark Editor, there is no problem related to the specimens being moved between sessions, because they share the coordinate system defined by the image (Richtsmeier *et* al., 1995). Thus, the absolute error was measured using the raw landmark coordinates from the digital endocasts, which are associated with a fixed coordinate space.

After calculating the MSD, charts of absolute error were constructed to observe the values for each landmark and specimens. Then, the frequency of error values was calculated on PAST, as well as a matrix of error distribution to help the visualization. Finally, to better understand the distribution of absolute error on each endocasts, maps of error distribution were created. These maps were constructed as follows: first, TPS.dig was used to mark the landmarks in 2 dimensions on each endocasts' 2D images; then, the coordinates (x,y) and the mean error from each landmark (averaged sides for bilateral landmarks) of a given endocasts were placed on PAST and a gridding function with multiquadratic algorithm was interpolated to develop a map of error distribution.

Discrepancy of Physical *vs* Digital data

A Procrustes Superimposition was performed on the physical and digital raw coordinates. Then Principal Component Analysis (PCA), and Cluster analysis by Unweighted Pair Group Method with Arithmetic average (UPGMA) were carried out on the Procrustes residuals. An additional UPGMA was performed on the PC variables which display a percentage of variation in shape space larger than 5% (PC1 to PC4). Using the same four PCs, the physical and digital overall variation in shape space was investigated the following way: first, the standard deviation (SD) of the PC variables from each replica was calculated for each endocast, then the SD values from the 4 PCs were summed for each endocast (physical and digital separately) and the variation within the resulting physical and digital values for each endocast were compared. This analysis was performed with PAST.

The overall pattern of variation was calculated per landmark and plotted to contrast physical and digital discrepancy patterns. For better observe the variation differences, matrixes of error distribution and maps of error for each endocast were obtained, as described above, for physical and digital data separately. To infer whether the variation is greater on physical or on digital samples, a ratio was calculated by dividing, for each landmark, the physical error values by the digital error values.

Plots of error per specimen for each landmark were obtained in order to compare the variation of physical and digital data with more detail. Dispersion graphs contrasting physical and digital landmark error values were computed for each specimen to test for correlation. Furthermore, to provide a better visualization of the landmarks divergence between physical and digital, the mean shapes from either physical and digital data were obtained with MorphoJ (Klingenberg, 2011) applying a discriminant function on the Procrustes residuals.

2.3.1. Shape Comparison

The comparison of shape between different organisms is the primary goal of geometric morphometrics. Thus, a shape comparison of the endocasts among the sample was accomplished, in order to complement this work. A PCA and a pairwise comparison were performed using the mean shapes from each endocast (physical + digital average).

3. RESULTS

3.1. ERROR AND VARIATION

3.1.1. Absolute Error

The mean absolute error within the digital sample is 0.86 ± 0.51 mm. The univariate statistics are resumed on table III. Values range from 0.15 to 3.44 mm, with the median being 0.74 mm and the values for the 25 and 75 percentiles being 0.53 mm and 1.06 mm, respectively. The majority of landmarks show discrepancies below 1.2 mm, as can be seen on figure 3.1a.

Table III – Univariate statistics for the digital sample without superimposition.

N	Mean	Std. Dev	Median	Min	Max	Percentile	
						25	75
152	0.86	0.51	0.74	0.15	3.44	0.53	1.06

Figure 3.1b illustrates the distribution of absolute error per landmark and per specimen. The mean values for each are listed on tables IV and V. The landmarks with greater values are the lateral sulcus, the supramarginal gyrus and the angular gyrus, all located on the parietal region. The human left angular gyrus is an outlier, with the maximum error value (3.44 mm), and the sequent maximum error being on the human left supramarginal gyrus (2.67 mm). In fact, the human's endocast (HUM) displays the greatest amount of error, in general (figure 3.1b) and in average (table V). The endocast displaying lesser error is the gibbon (GIB).

Table IV – Mean absolute error for each landmark. Left (L) and right (R) values are shown separately.

Landmark	Absolute error (mean ± s.d. mm)
FPL	0.68 ± 0.61
FPR	0.69 ± 0.58
OPL	0.60 ± 0.29
OPR	0.66 ± 0.34
TPL	0.59 ± 0.28
TPR	0.61 ± 0.23
CPL	0.75 ± 0.26
CPR	0.84 ± 0.30
BCL	0.64 ± 0.20
BCR	0.68 ± 0.24
LSL	0.97 ± 0.43
LSR	1.36 ± 0.68
SGL	1.40 ± 0.63
SGR	1.06 ± 0.42
AGL	1.40 ± 0.88
AGR	1.30 ± 0.45
CS	0.75 ± 0.32
PS	0.72 ± 0.27
IOP	0.56 ± 0.21

Table V – Mean absolute error for each endocast.

Endocast	Absolute error (mean ± s.d. mm)
BON	0.92 ± 0.34
CHIM	0.81 ± 0.39
CHIF	0.98 ± 0.47
GIB	0.49 ± 0.27
GOR	0.94 ± 0.39
HUM	1.40 ± 0.75
ORG	0.79 ± 0.36
SIA	0.52 ± 0.25

The distribution of error on each endocast can be visualized on figure 3.2. An overall pattern with greater error around the parietal area and lesser error around the poles (frontal, occipital, temporal, cerebellar) and the sagittal landmarks can be easily noticed. However there are some exceptions. Central sulcus on the male chimp (CHIM) and human (HUM) endocasts display larger amount of error, in relation to the other casts' pattern. HUM and the orangutan (ORG) also display larger error on the frontal poles, and the gorilla (GOR) on the occipital.

Figure 3.3 shows the absolute error values for each landmark. Frontal poles exhibit error lesser than 1 mm, except those of HUM and ORG, both on left and right sides. The occipital poles with error larger than 1 mm are those of GOR and the right poles of BON and CHIF. Considering the temporal poles, only those of HUM exceed (left) or are closer (right) to 1 mm. Cerebellar poles of CHIM, HUM and ORG (right) exceed that value as well. Broca's cap and the sagittal landmarks also display error values lesser than or equal to 1 mm, with only the HUM central sulcus error being larger (1.31 mm). The internal occipital protuberance is the landmark displaying the smallest error mean (table IV). The greater amount of error, as stated above, is located on the parietal area (lateral sulcus, supramarginal and angular gyri). From these landmarks, the left lateral sulcus is the one with the lesser error mean (table IV). Supramarginal and angular gyri both display the greater mean values but only on the left side (table IV), mainly because of the human endocast. HUM and CHIF display error larger than 1 mm on all those three landmarks, both left and right. But the error is also larger among the other specimens. Only GIB, ORG and SIA display smaller values of error on the parietal area. These endocasts display the smaller absolute error means (table V).

Some discrepancy on the bilateral landmarks between the left and right can be noted on figure 3.3. The landmarks displaying most discrepancy are the ones with larger absolute error (LS, SG and AG). Regarding the lateral sulcus, the major discrepancy is on CHIF (difference of 0.92 mm) and GOR (1.68 mm), with larger error on the right side. Regarding the supramarginal gyrus, the larger disparity is on BON (1.04 mm) and HUM (1.14 mm), with larger error on the left side. The angular gyrus of HUM is the landmark displaying the greater difference (2.10 mm) with larger error on the left side.

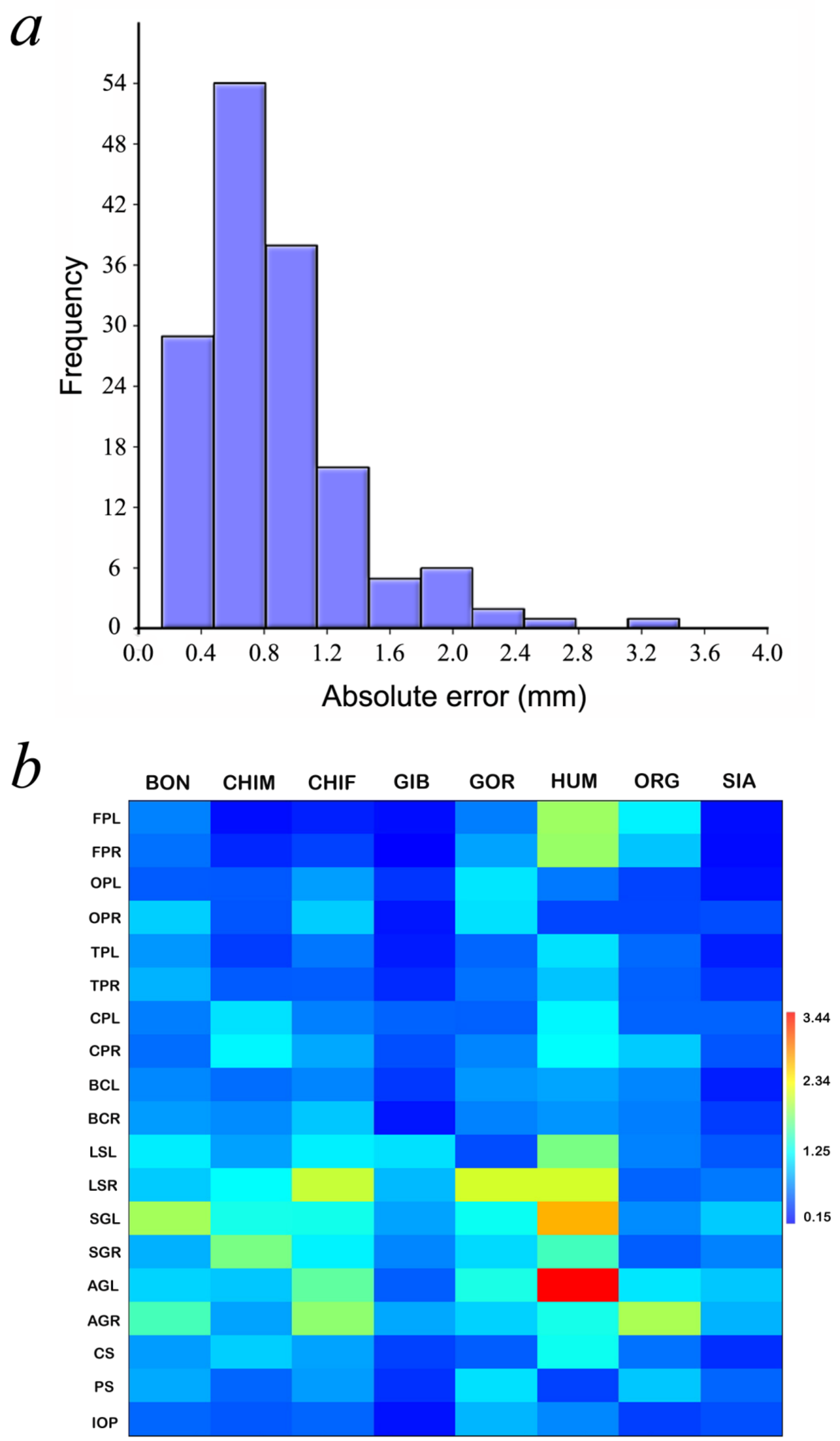

Figure 3.1. Histogram showing the frequency of the absolute error values (a) and matrix of distribution of those values throughout the sample (b). See appendix A for the values.

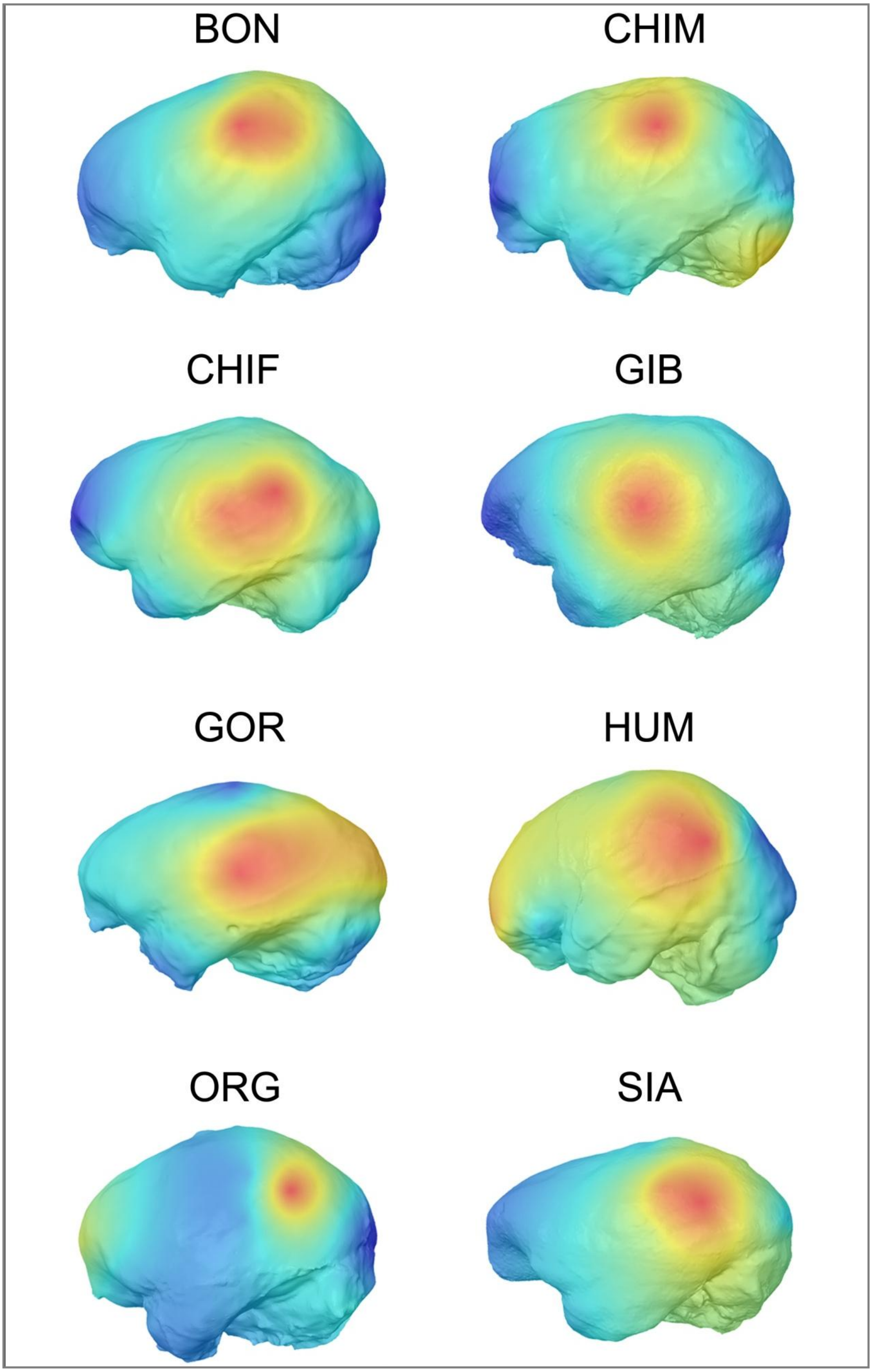

Figure 3.2. Error maps exhibiting the distribution of absolute error for each specimen (averaged sides). Error increases from blue to red. Note that the scales are specific to each endocast.

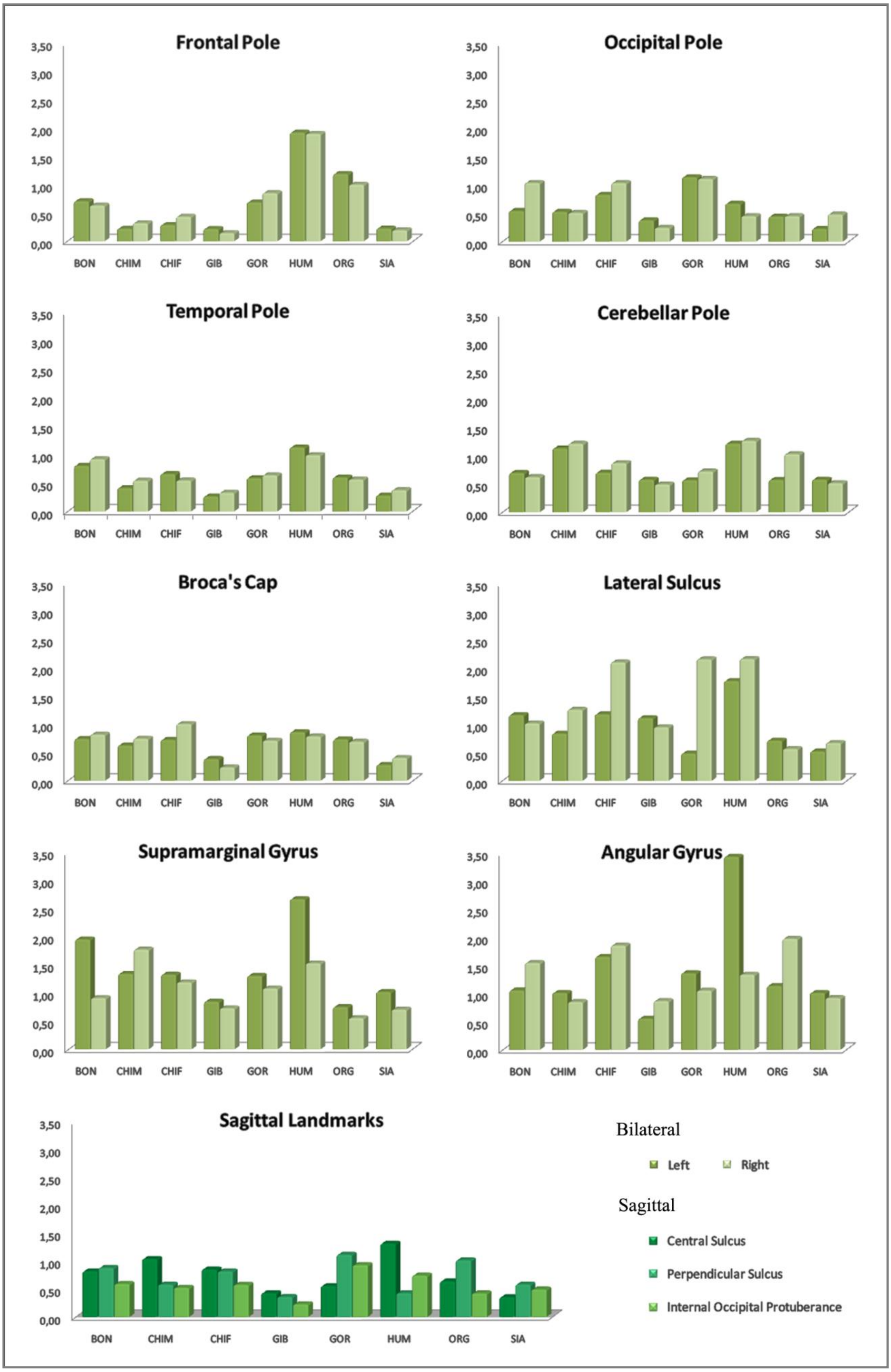

Figure 3.3. Absolute error values fluctuation per specimen for each landmark. Values can be consulted on appendix A.

3.1.2. Physical *vs* Digital

Variation in Shape Space

The PCA plot taking the whole sample (physical + digital) into account is shown on figure 3.4. The first two PCs represent 55.6% of the variance. PC1 explains 39.8% of the variance and PC2 explains 15.8% of the variance. The different specimens are clearly separated, and the replicas group together. However, for some specimens, there is a minor separation between the physical and digital replicas. For example on CHIF the division is clear. This separation can also be detected from the UPGMA phenograms (figure 3.5 a, b), on which one can see that some specimens part from two main branches. On both phenogram there is a CHIF replica that is set apart from the others, specially on the UPGMA performed with the PC1 to PC4 variables (figure 3.5b), where this outlier is closer to SIA. Apart for this singularity both phenograms are very similar.

UPGMA phenograms display mainly the variation that occurs along PC1. HUM is well separated from the rest of the specimens. BON and ORG are closer to each other than to the rest of the sample. CHIF appears closer to BON on the PCA, but on the phenogram it is closer to SIA, which is mainly caused by the outlier digital replica, as figure 3.5b shows. CHIM seems to be at the same distance from CHIF and SIA. GIB is closer to GOR than it is to SIA. As this distribution of the specimens on shape space is related to shape, it is deeper analysed on section 3.2 (Shape Comparison).

Analyzing the variation within the first four PCs for each separate replica, digital replicas display larger values than the physical ones (figure 3.6). But the difference is not significant according to a Mann-Whitney test (p = 0.08).

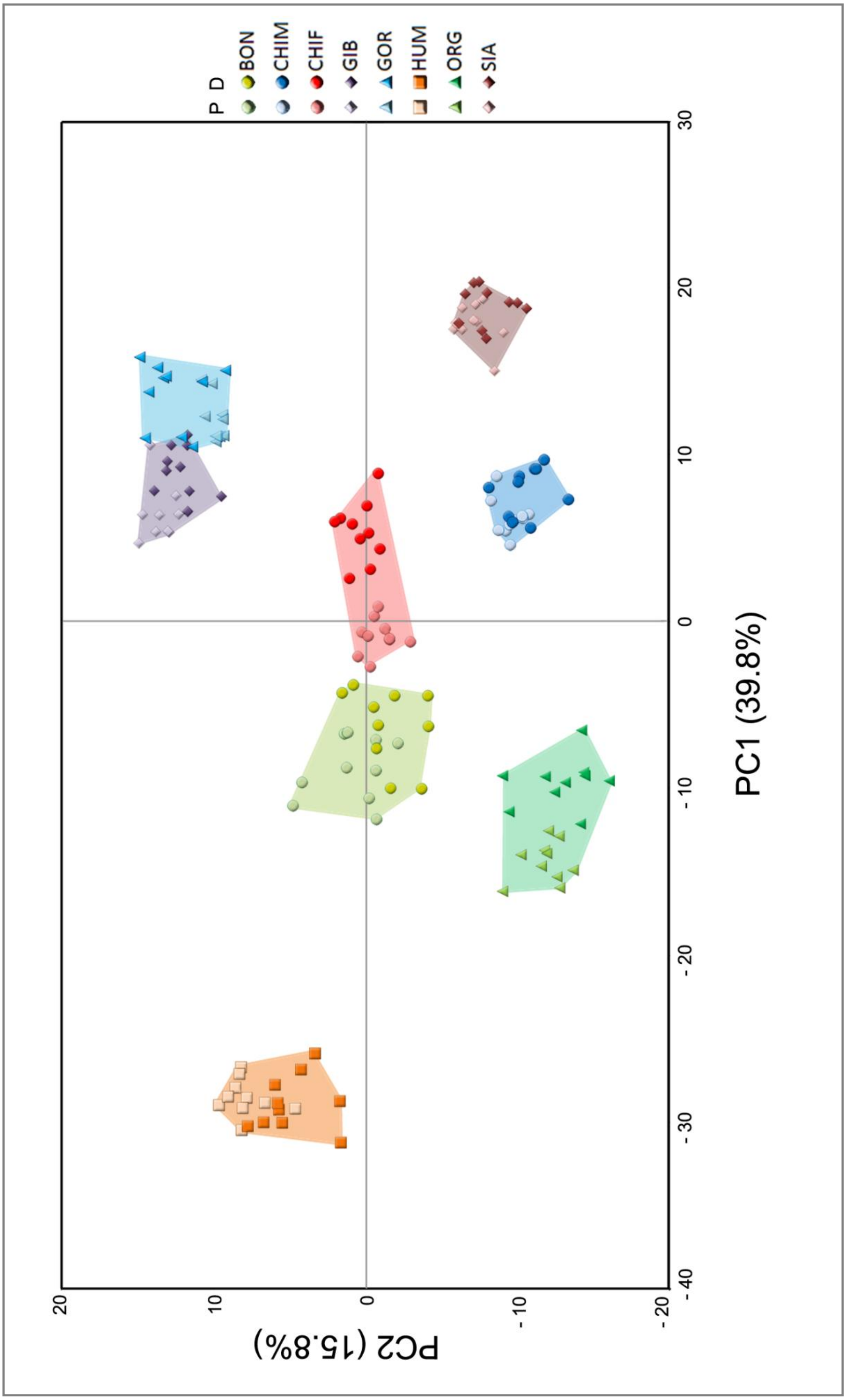

Figure 3.4. Variation in shape space after Procrustes superimposition (pooled physical and digital samples). The plot shows the distribution of each replica.

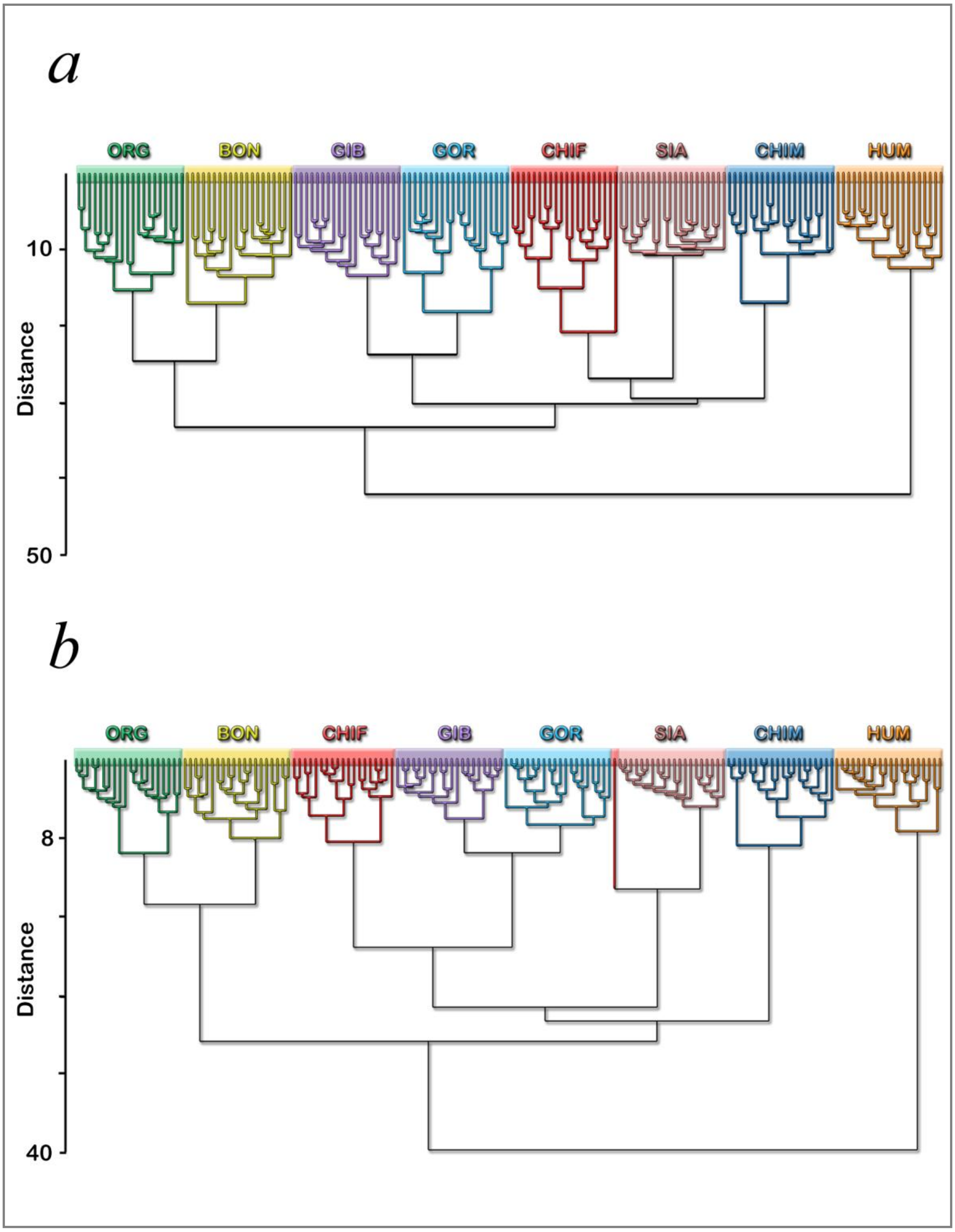

Figure 3.5. UPGMA phenograms using (a) the Procrustes coordinates (cophenetic correlation coefficient = 0.88) and (b) the first four principal components (which display a percentage of variation larger than 5%, see appendix B) (coph. corr. coeff. = 0.88).

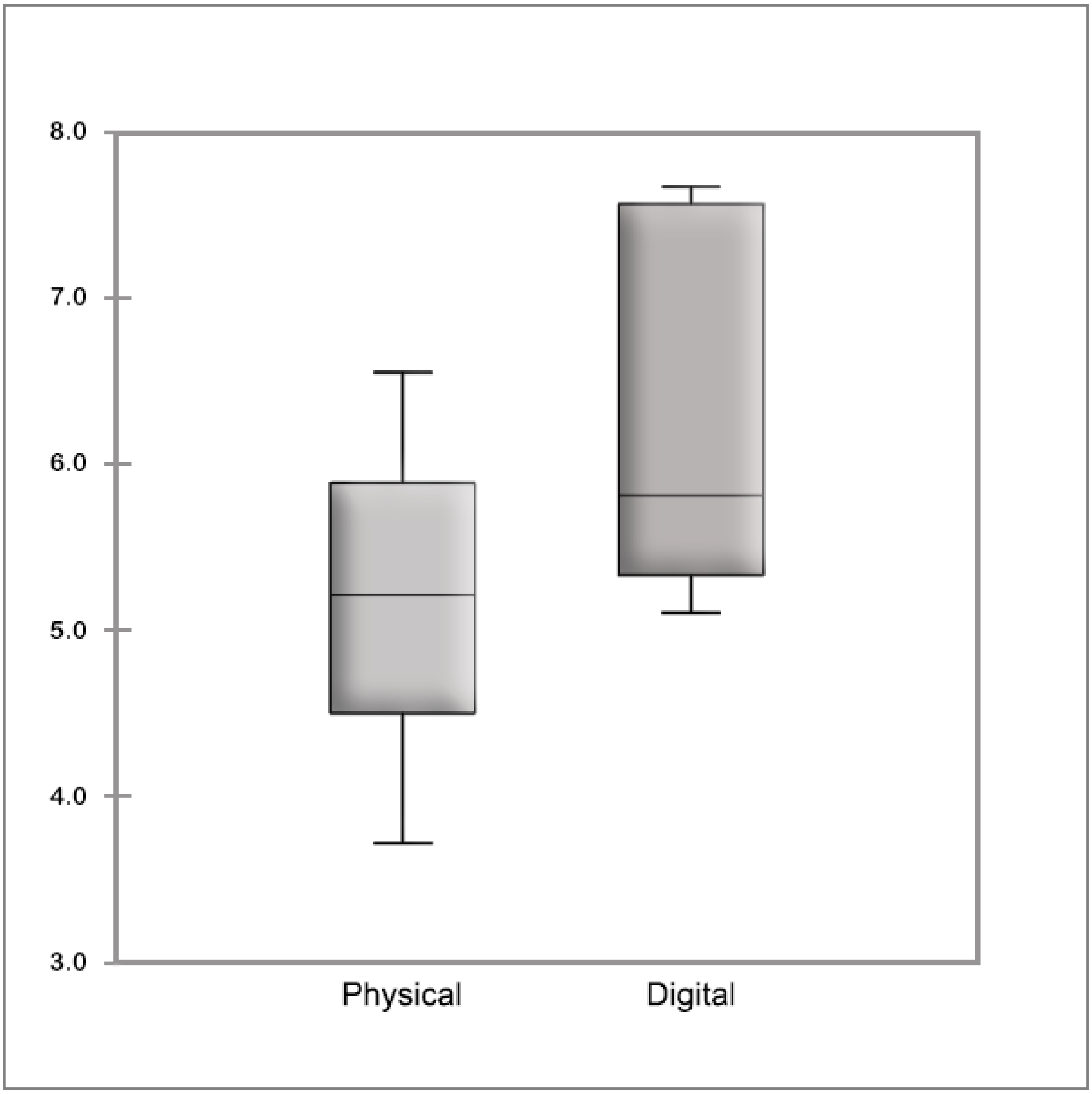

Figure 3.6. Distribution of the summed discrepancy in the physical and digital superimposed data for the first four principal components (variation > 5%).

Physical and Digital Discrepancy

Considering the bilateral landmarks averaged, the pattern of error of physical and digital samples is similar on the majority of landmarks (figure 3.7a). However, when the bilateral landmarks are considered separately (figure 3.7b) the patterns diverge. The landmarks that differ more are the frontal poles and the parietal landmarks.

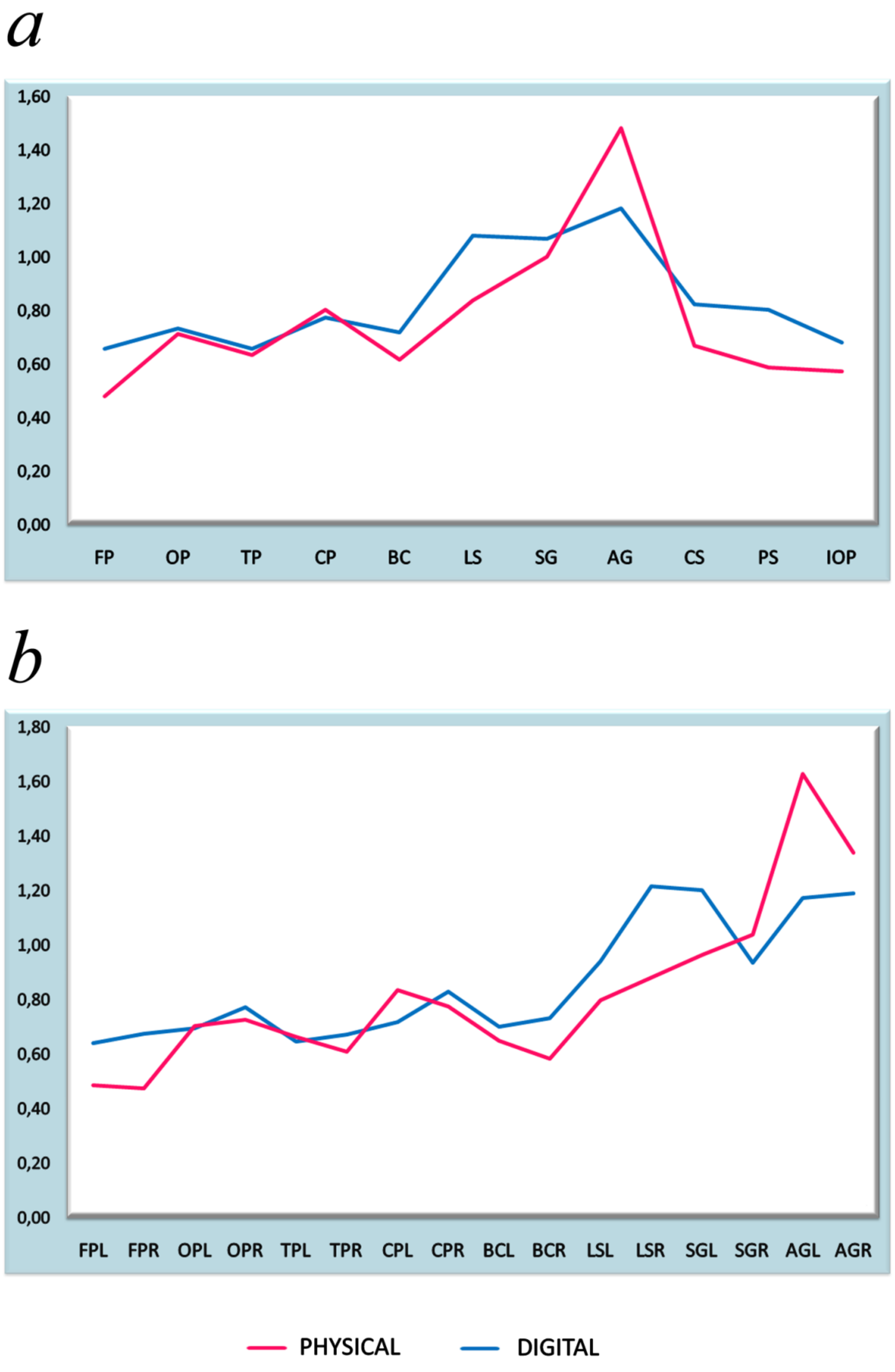

Figure 3.7. Comparison of landmark variation patterns within the physical and the digital samples, considering the bilateral landmarks averaged or (a) separately (b).

Although some landmarks show larger variation values in the physical sample, and others have larger variation on the digital, in general, there are more landmarks displaying greater variation on the digital sample (figure 3.8). Also, the overall variation mean of the digital sample (0.85 ± 0.31) is larger than that of the physical (0.79 ± 0.31).

The variation mean values for each landmark and specimen are listed on tables VI and VII, respectively. The distribution of variation values per landmark and per specimen are shown on figure 3.9, for both physical and digital samples.

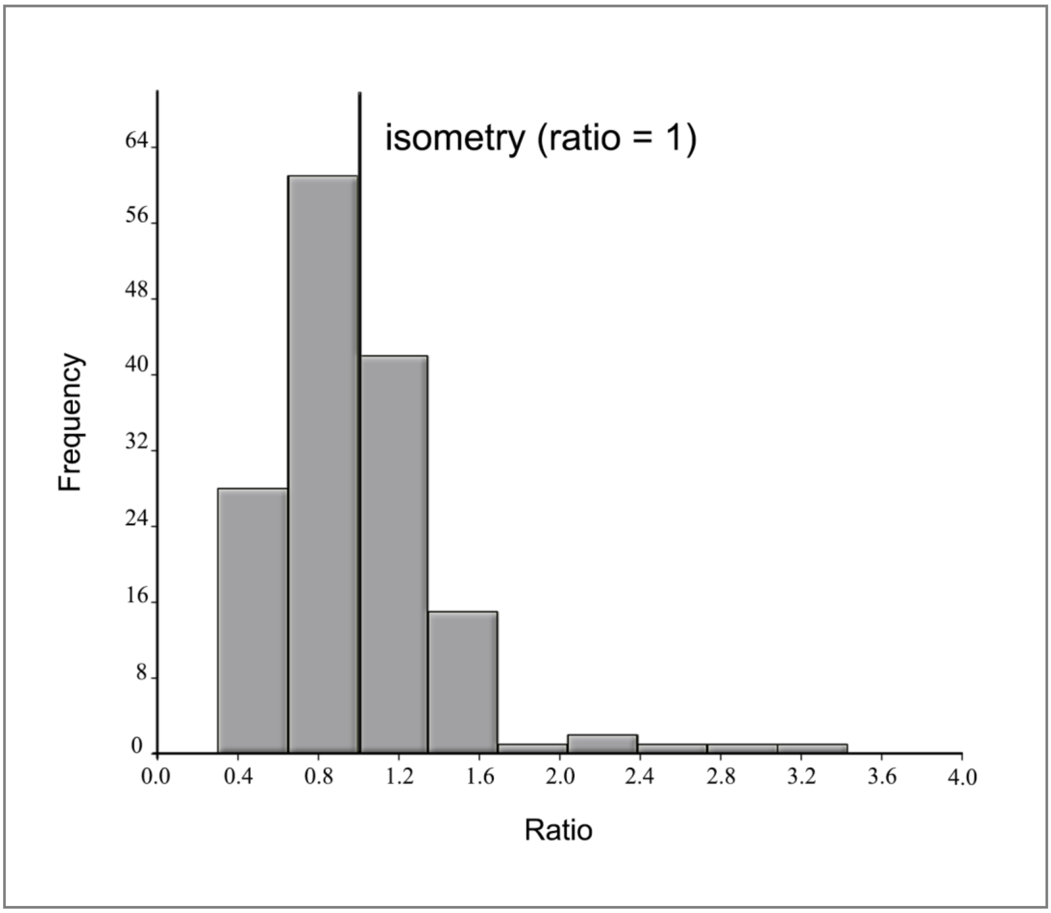

Figure 3.8. Histogram showing the ratio between the physical and digital discrepancy values after superimposition (the same distribution should give a result of 1).

Both on physical and digital samples, the landmarks displaying greater variation means are those located on the parietal (LS, SG and AG). The lateral sulci (left and right) and the left supramarginal gyrus display larger mean error on the digital sample, and the right SG and the angular gyri (left and right) display larger mean error on the physical sample (table VI). The same can be observed on the other landmarks: some having larger mean variation on the physical sample and some on the digital. Differences between left and right mean error values can also be noticed.

Table VI – Mean variation for each landmark. Left (L) and right (R) values are shown separately.

Landmark	Variation (mean ± s.d.)	
	Physical	Digital
FPL	0.49 ± 0.13	0.64 ± 0.22
FPR	0.47 ± 0.09	0.67 ± 0.21
OPL	0.70 ± 0.21	0.70 ± 0.21
OPR	0.73 ± 0.26	0.77 ± 0.28
TPL	0.66 ± 0.11	0.65 ± 0.18
TPR	0.61 ± 0.10	0.67 ± 0.11
CPL	0.83 ± 0.13	0.72 ± 0.11
CPR	0.77 ± 0.11	0.83 ± 0.14
BCL	0.65 ± 0.20	0.70 ± 0.12
BCR	0.58 ± 0.14	0.73 ± 0.19
LSL	0.80 ± 0.33	0.94 ± 0.34
LSR	0.88 ± 0.44	1.22 ± 0.45
SGL	0.96 ± 0.29	1.20 ± 0.28
SGR	1.04 ± 0.35	0.94 ± 0.27
AGL	1.63 ± 0.81	1.17 ± 0.38
AGR	1.34 ± 0.54	1.19 ± 0.34
CS	0.67 ± 0.29	0.82 ± 0.19
PS	0.59 ± 0.18	0.80 ± 0.17
IOP	0.57 ± 0.16	0.68 ± 0.13

Table VII – Mean variation for each endocast.

Endocast	Variation (mean ± s.d.)	
	Physical	Digital
BON	0.81 ± 0.28	0.88 ± 0.26
CHIM	0.83 ± 0.60	0.76 ± 0.27
CHIF	0.75 ± 0.48	1.01 ± 0.28
GIB	0.92 ± 0.40	0.78 ± 0.33
GOR	0.77 ± 0.35	0.87 ± 0.32
HUM	0.57 ± 0.25	0.91 ± 0.34
ORG	0.87 ± 0.35	0.79 ± 0.26
SIA	0.78 ± 0.32	0.76 ± 0.27

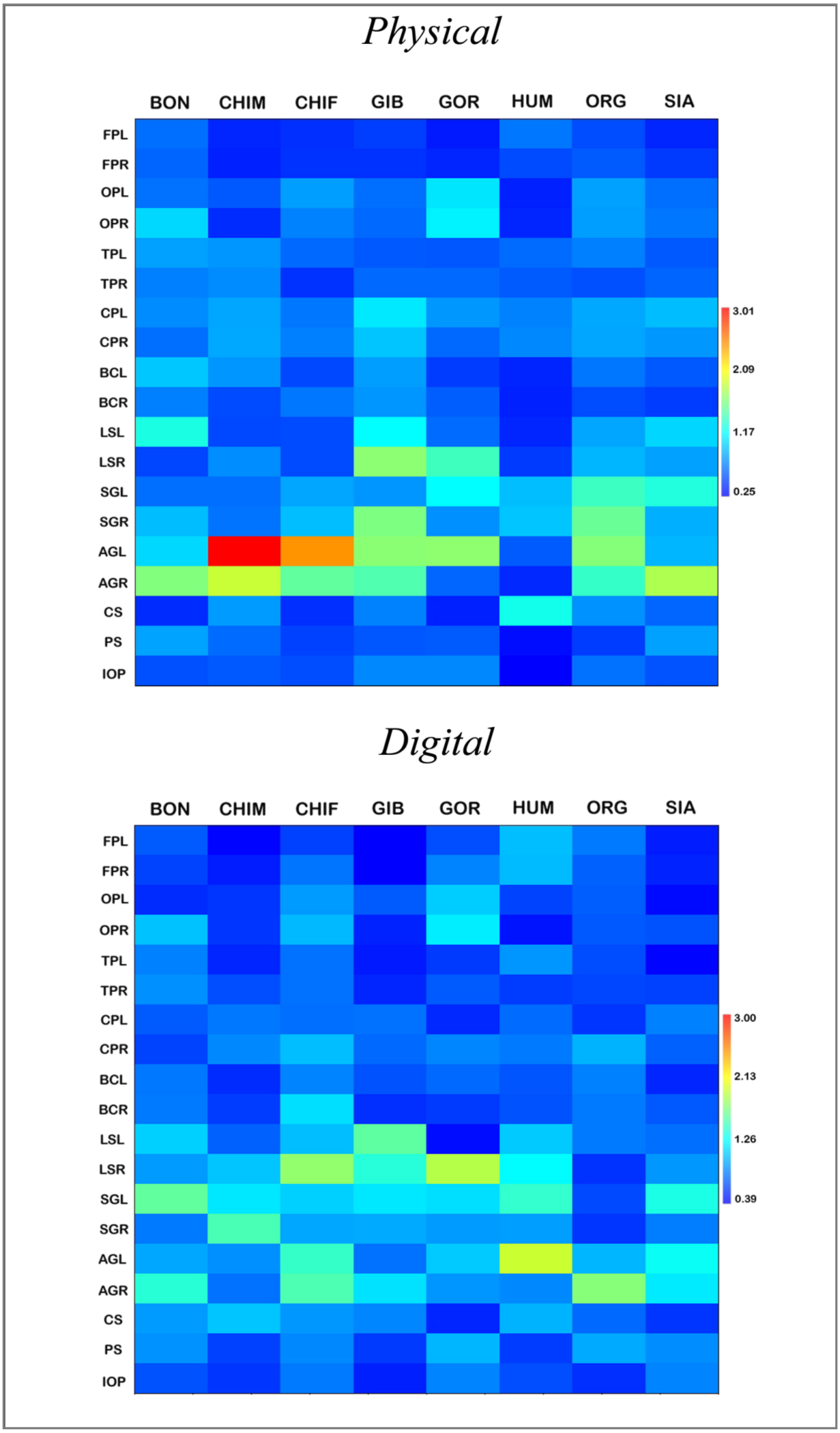

Figure 3.9. Distribution of physical and digital error after Procrustes superimposition, according to a chromatic scale in order to visualize the major patterns. The scales are similar, for comparison. See appendix C for the original values.

The largest error values on the physical sample belong to the left angular gyrus of CHIM (3.01) and CHIF (2.48). On the digital sample the largest error values are those of HUM left angular gyrus (1.95) and the right lateral sulcus of GOR (1.88).

Taking the endocasts into account, the ones displaying larger mean variation on the physical sample are CHIM, GIB, ORG and SIA, with GIB exhibiting the largest value. The other four specimens (BON, CHIF, GOR and HUM) have greater mean error values on the digital sample, with the largest value belonging to CHIF. The specimens having greater difference between physical and digital mean values are HUM and CHIF.

The maps on figure 3.10 illustrate the landmark error distribution within each endocast, confronting physical and digital patterns. Differences between physical and digital versions of the same specimen are easily visualized on the color pattern. In general, the patterns are somewhat variable, but all maps (except the physical HUM) exhibit larger error on the parietal region. The most similar patterns are those of SIA and the most different are those of HUM and CHIM.

BON displays larger error on the angular gyrus on the physical sample and on the supramarginal gyrus on the digital. On CHIM, the error value of the angular gyrus is much larger on the physical than on the digital, and the digital display greater error on the supramarginal gyrus. CHIF has greater error on the angular gyrus both on physical and digital samples, but the digital one displays also greater error on the lateral sulcus. On the physical sample, GIB exhibits larger error on LS, SG and AG, but, in comparison, on the digital sample the specimen shows larger values on LS and lesser values on AG. Both physical and digital versions of GOR map display greater error on the occipital poles and on the parietal region, with the divergence resulting from a larger error on AG for the physical sample and on LS for the digital sample. On HUM, whereas the physical version displays greater error mainly on the central sulcus and little on the rest of the landmarks, the digital version also exhibits larger error on frontal poles and on the parietal landmarks. On ORG, the angular gyrus is the landmark displaying larger error on both physical and digital samples, with the addition of supramarginal gyrus on the physical. SIA exhibits greater error mainly on SG and AG on both versions.

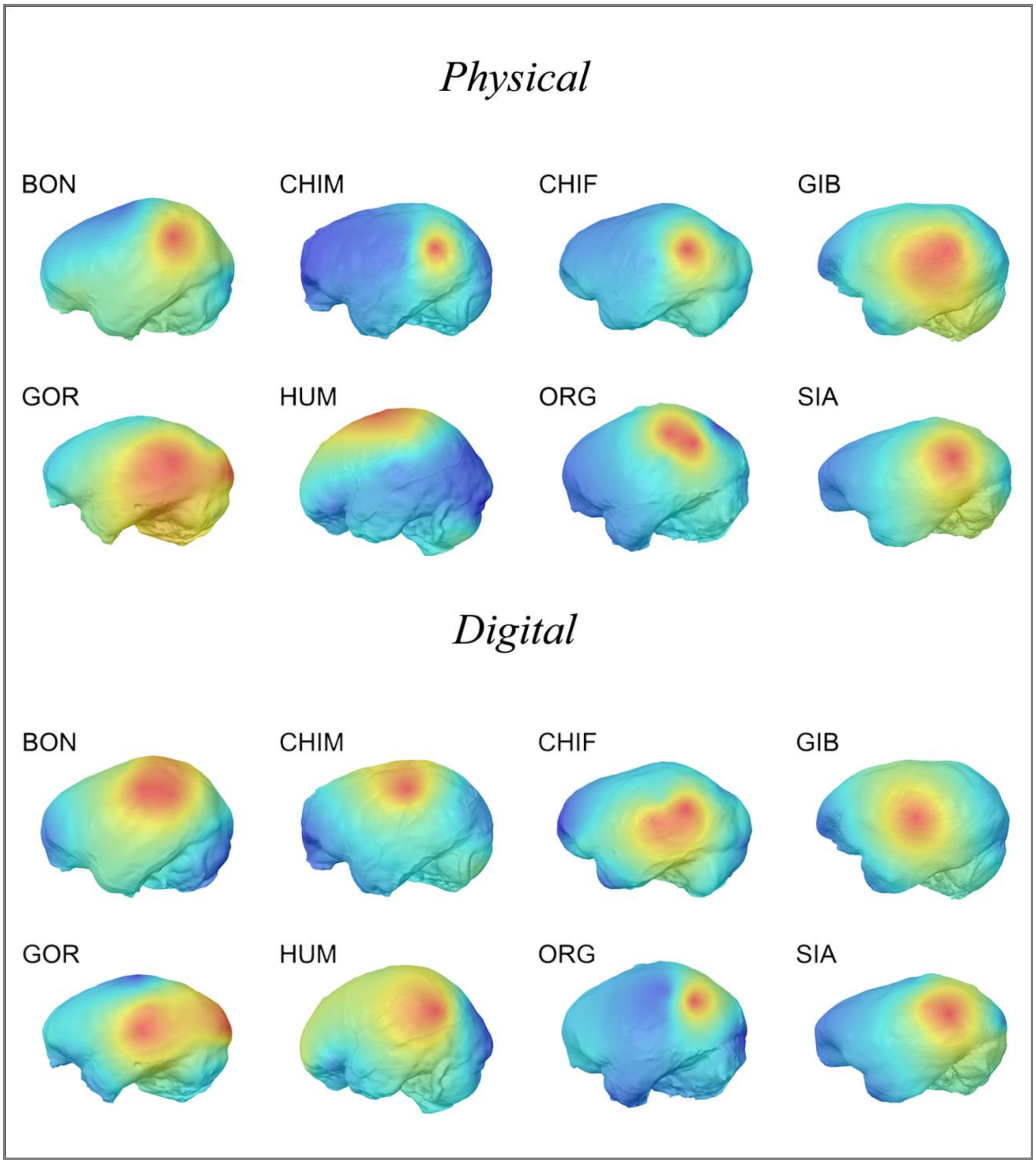

Figure 3.10. Maps of distribution of the error of physical and digital samples after Procrustes superimposition for each specimen (averaged sides). Error increases from blue to red. Note that the scales are specific to each endocast.

Next the difference between the discrepancy values of physical and digital samples is analyzed specimen by specimen. The results for each endocast are shown on figures 3.11 to 3.18.

Bonobo

According to figure 3.11a, BON displays larger difference between physical and digital on the right lateral sulcus, left supramarginal gyrus, right angular gyrus and the central sulcus. The right AG is the landmark displaying greater error on the physical sample (error = 1.64). On the digital sample the error values is slightly smaller (1.40). On the left side, the AG exhibits smaller values of error, being also larger on physical (1.03) than on digital (0.96). The left SG has the larger error value among the digital sample (1.59), considerably larger than that of the physical sample (0.65). However, the right SG, error is somewhat greater on the physical (0.93) than on the digital (0.81) sample. Lateral sulcus displays larger error values on the left side, with larger side differences on the physical sample. Plus, LS exhibits larger error on physical on the left side and on digital on the right side. The same pattern can be seen on the occipital pole. All the sagittal landmarks show larger error on the digital sample, with the central sulcus displaying the greater difference.

The error values from physical and digital are poorly correlated (R^2=0.23; figure 2.11b), with the left SG as an outlier. Wireframes demonstrate that the greater discrepancies between the two methods are on the AG, specially the right one, left Broca's cap, right LS and on CS.

Chimpanzee Male

From all CHIM's landmarks the angular gyrus is the one displaying greater error on the physical sample, and greater difference between physical and digital samples, both on the left (3.01) and on the right (1.89) sides (figure 3.12a). By contrast, on the digital sample the error values are smaller, and so is the difference between left (0.88) and right (0.78). The other landmarks exhibiting larger differences between physical and digital error values, LS, SG and CS, display greater values on the digital sample. Broca's cap, shows larger error values on physical (0.79) with greater difference from the digital (0.54), on the left side, and larger error on the digital (0.60) sample, with smaller difference from the physical (0.52) on the right side.

By figure 3.12b, there is no correlation between physical and digital error values (R^2= 0.04), what can be due to the AG which is an extreme outlier. This landmark is the one with more discrepancy between the physical and digital mean shapes, especially on the left side (figure 3.12c).

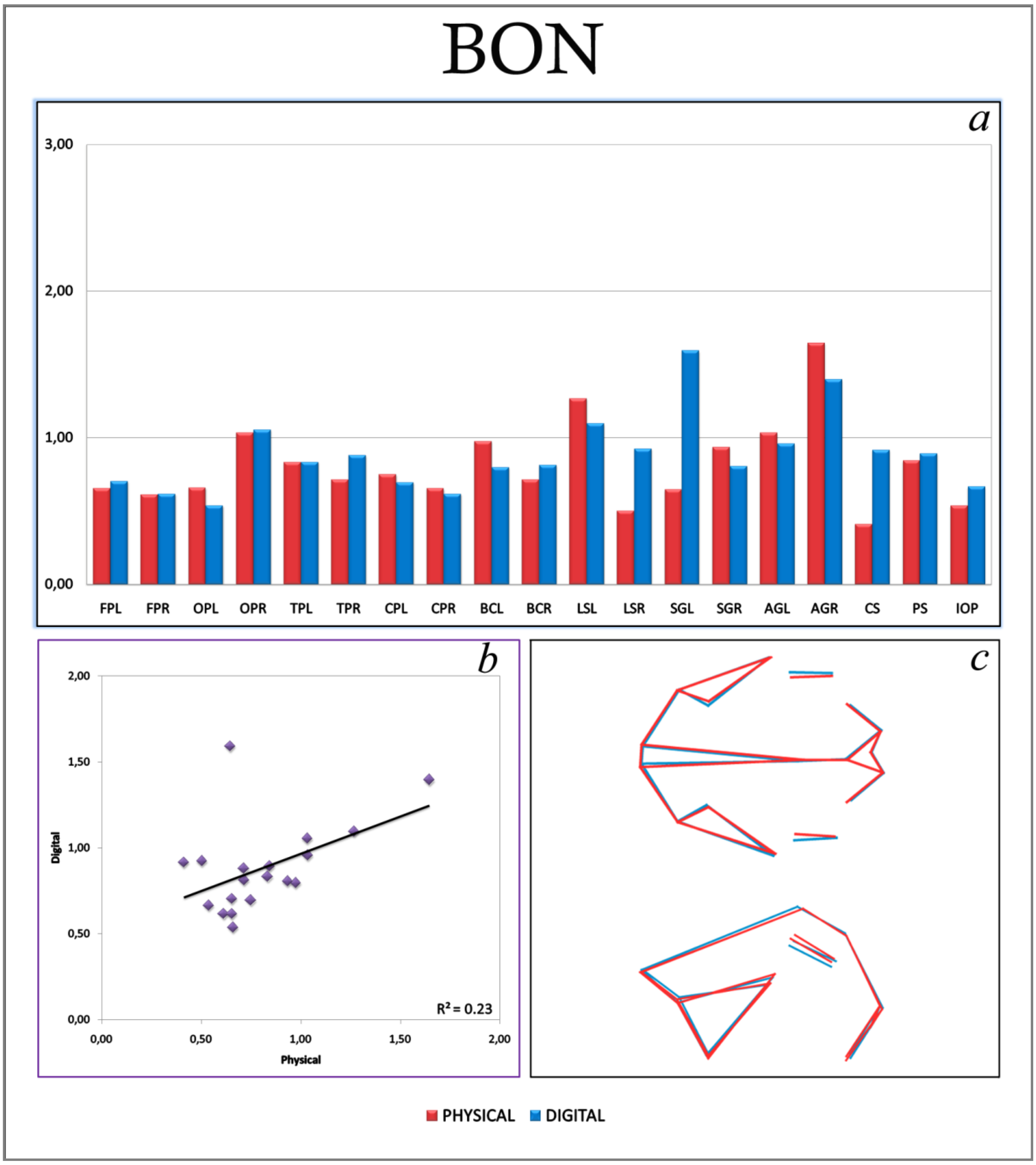

Figure 3.11. Differences between physical and digital variation on bonobo. Charts compare (a) and correlate (b) error values per landmark. Wireframes illustrate the pairwise comparison between physical and digital mean shapes, showing the superior (above, left side up) and lateral (below) views.

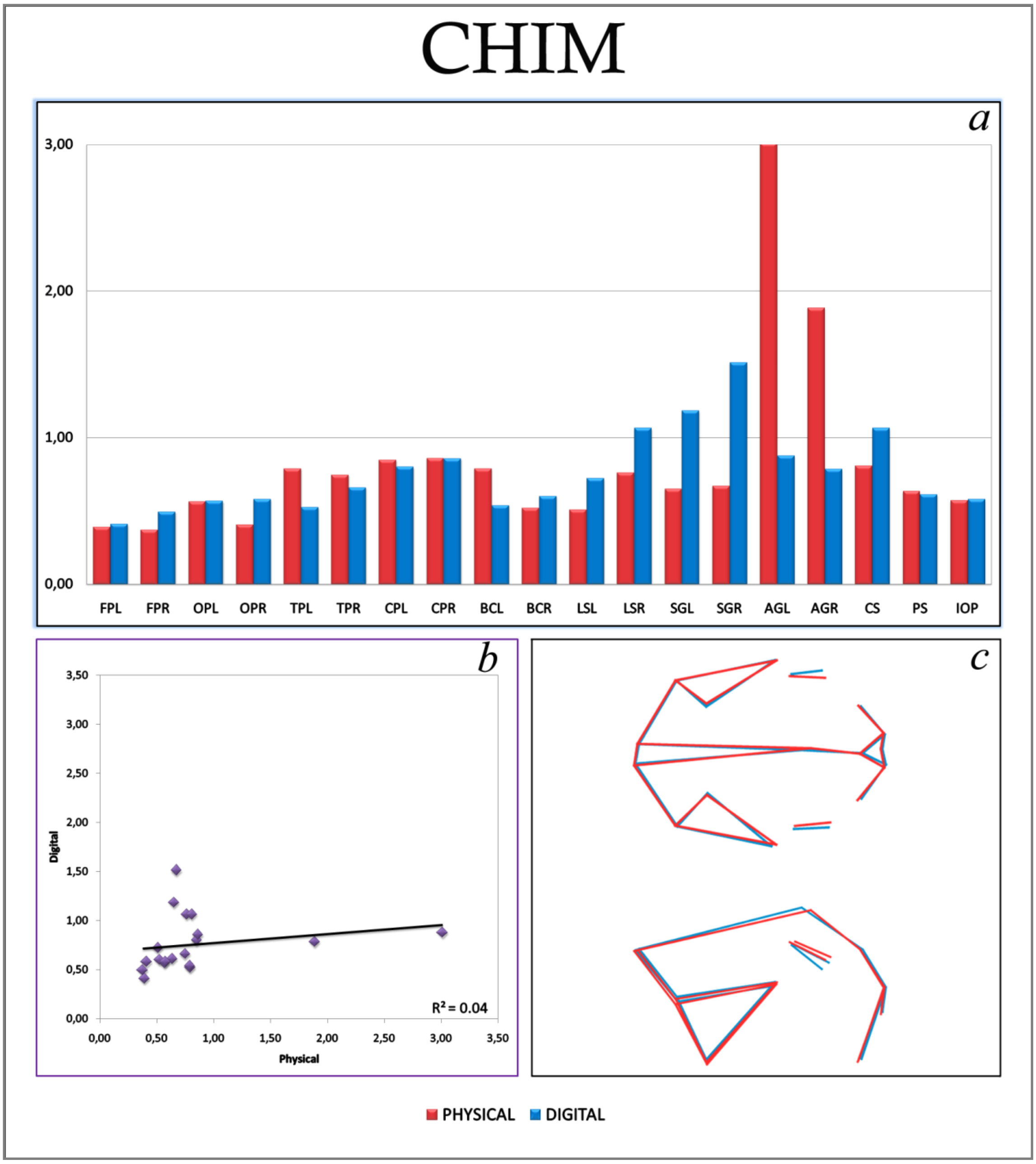

Figure 3.12. Differences between physical and digital variation on the male chimpanzee. Charts compare (a) and correlate (b) error values per landmark. Wireframes illustrate the pairwise comparison between physical and digital mean shapes, showing the superior (above, left side up) and lateral (below) views.

Chimpanzee Female

The majority of landmarks on CHIF exhibit considerable discrepancy between physical and digital error values (figure 3.13a), with almost all displaying larger error on the digital sample. Lateral sulcus displays the largest error value of the digital sample, on the right side (1.76). Although the difference from the left LS (1.04) is considerable, both show great discrepancy from the physical sample, on which LS display the same error value on both sides (0.52). The left AG is the only landmark displaying larger error on the physical sample (2.48) comparing to the digital (1.45). On the right side AG displays equal error values (1.52) for both samples.

The correlation between physical and digital error values is very small (R^2=0.31; figure 3.13b). Greater differences in locating landmarks on physical or on digital landmarks are on LS, right AG, PS and IOP (figure 3.13c).

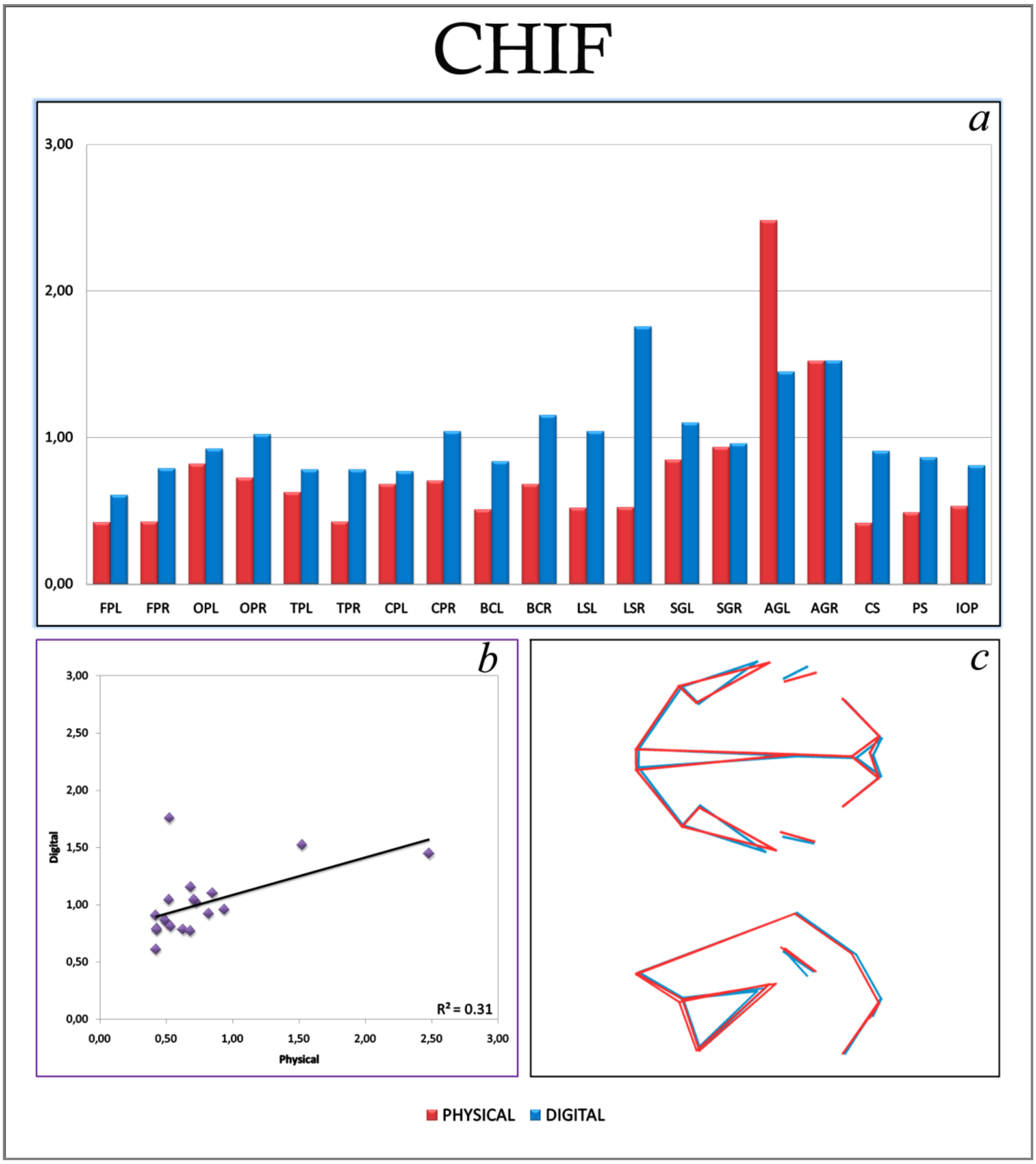

Figure 3.13. Differences between physical and digital variation on the female chimpanzee. Charts compare (a) and correlate (b) error values per landmark. Wireframes illustrate the pairwise comparison between physical and digital mean shapes, showing the superior (above, left side up) and lateral (below) views.

Gibbon

GIB exhibits larger error values on the physical sample on the majority of landmarks (figure 3.14a). Greater discrepancies between physical and digital error values are located on the parietal landmarks. AG displays larger error on the left (1.67) than on the right (1.46) on the physical sample, but larger error on the right (1.16) than on the left (0.78) on the digital. LS and SG also display great divergence between left and right: both landmarks have larger error values on the left side, on the digital sample, and on the right side on the physical sample.

The value for correlation, although also small, is somewhat larger than those of the previous specimens, (R^2=0.48; figure 3.14b). Greater divergence between physical and digital mean shapes is found on SG, mainly the right one, according to the pairwise comparison (figure 3.14c). The wireframes also show some asymmetry on the specimen, which is better seen on SG, AG and LS.

Gorilla

On GOR, greater discrepancies between physical and digital error values are found on the frontal poles, right lateral sulcus and perpendicular sulcus, with larger values on the digital sample, and on the left angular gyrus, with larger values on the physical sample (figure 3.15a). LS and AG also exhibit large discrepancies between left and right values. The largest difference between sides is displayed by LS, with larger error on the right side, both on physical (1.40) and digital (1.88) samples. On the digital sample, this landmark exhibits both the largest (on the right) and the smallest (on the left: 0.44) error values. A similar pattern is exhibited by the AG, which displays the largest error value for the physical sample, on the left side (1.69), with considerable difference from the right side (0.77). On the digital sample the difference between sides is smaller (1.08 left; 0.90 right).

A little correlation exists between error values of physical and digital samples (R^2=0.51; figure 3.15b). The wireframe comparison shows that the major discrepancy between physical and digital methods is in locating SG, AG, TP and BC on the left side, and LS on the right (figure 3.15c).

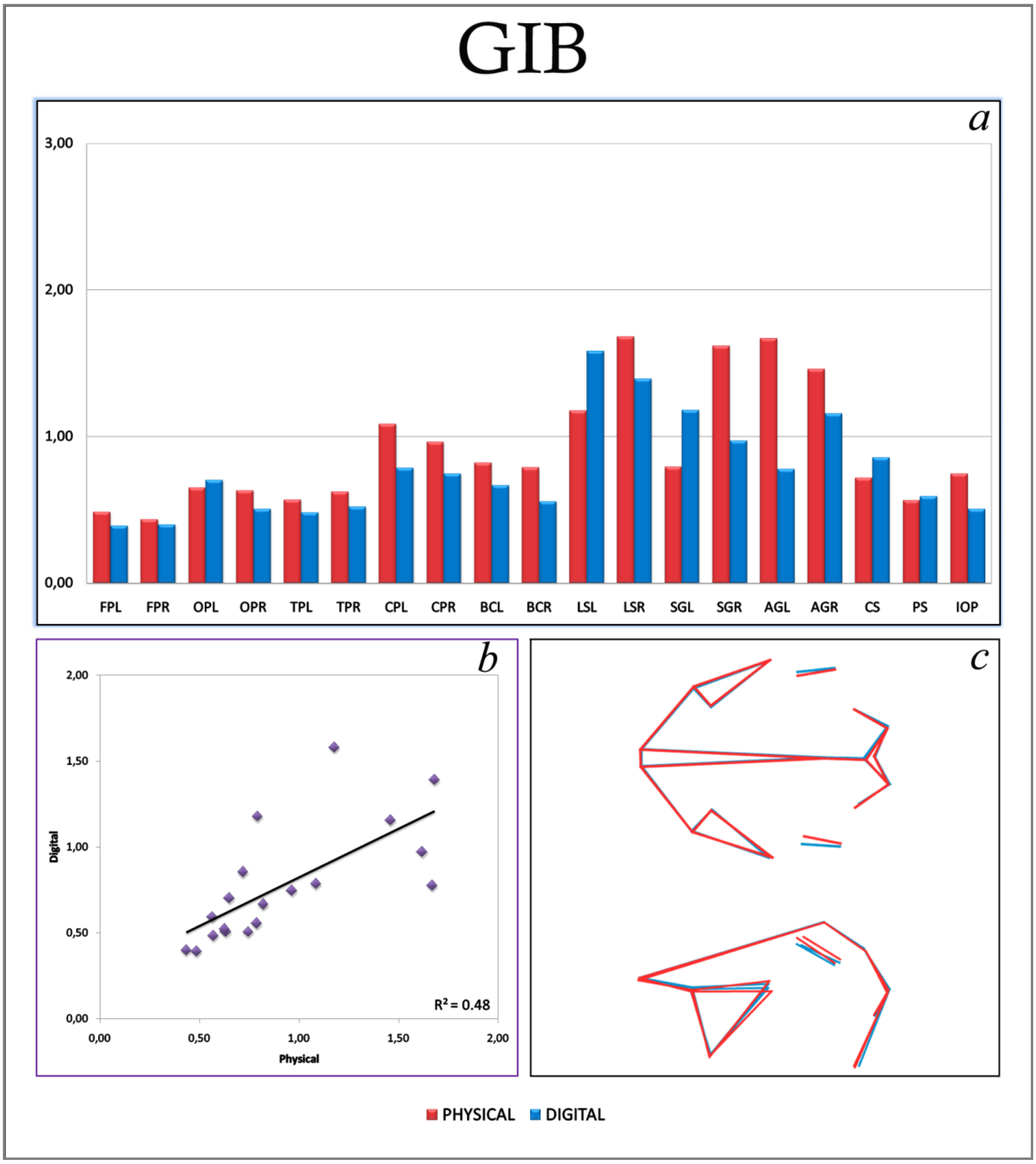

Figure 3.14. Differences between physical and digital variation on gibbon. Charts compare (a) and correlate (b) error values per landmark. Wireframes illustrate the pairwise comparison between physical and digital mean shapes, showing the superior (above, left side up) and lateral (below) views.

Human

According to figure 3.16a, HUM exhibits larger error values, on the digital sample, on all landmarks except the central sulcus, which displays the greatest error value of the physical sample (1.24). AG exhibits the largest error of the digital sample on the left side (1.95), and the greater discrepancies both between physical and digital and left and right values. Other landmarks displaying great discrepancy between physical and digital are FP, BC, LS, left SG, PS and IOP.

The error values show almost no correlation (R^2=0.12; figure 3.16b), but despite the considerable differences between physical and digital error values, the mean shapes from each sample are very similar, exhibiting only little difference on FP and CS (figure 3.16c).

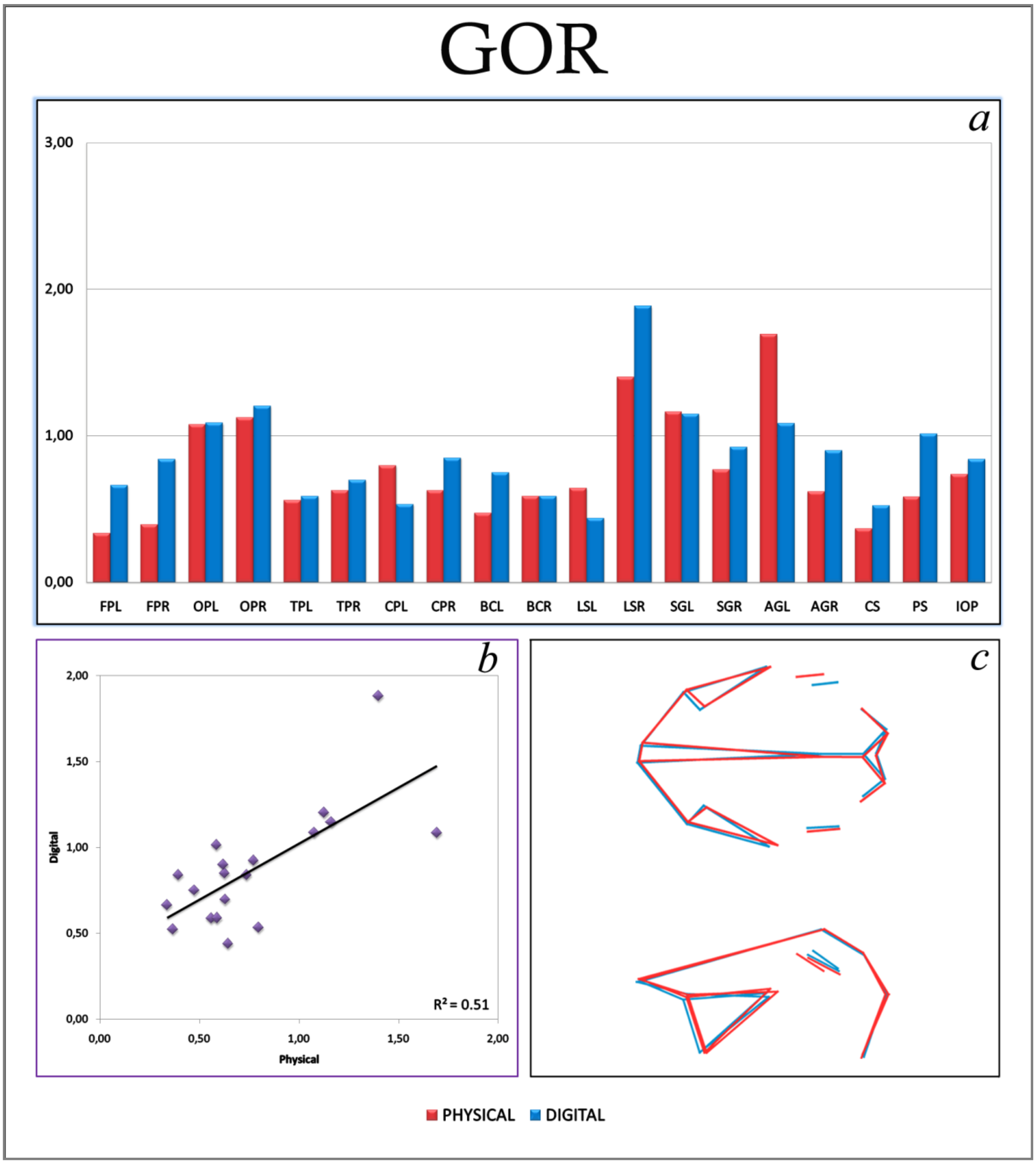

Figure 3.15. Differences between physical and digital variation on gorilla. Charts compare (a) and correlate (b) error values per landmark. Wireframes illustrate the pairwise comparison between physical and digital mean shapes, showing the superior (above, left side up) and lateral (below) views.

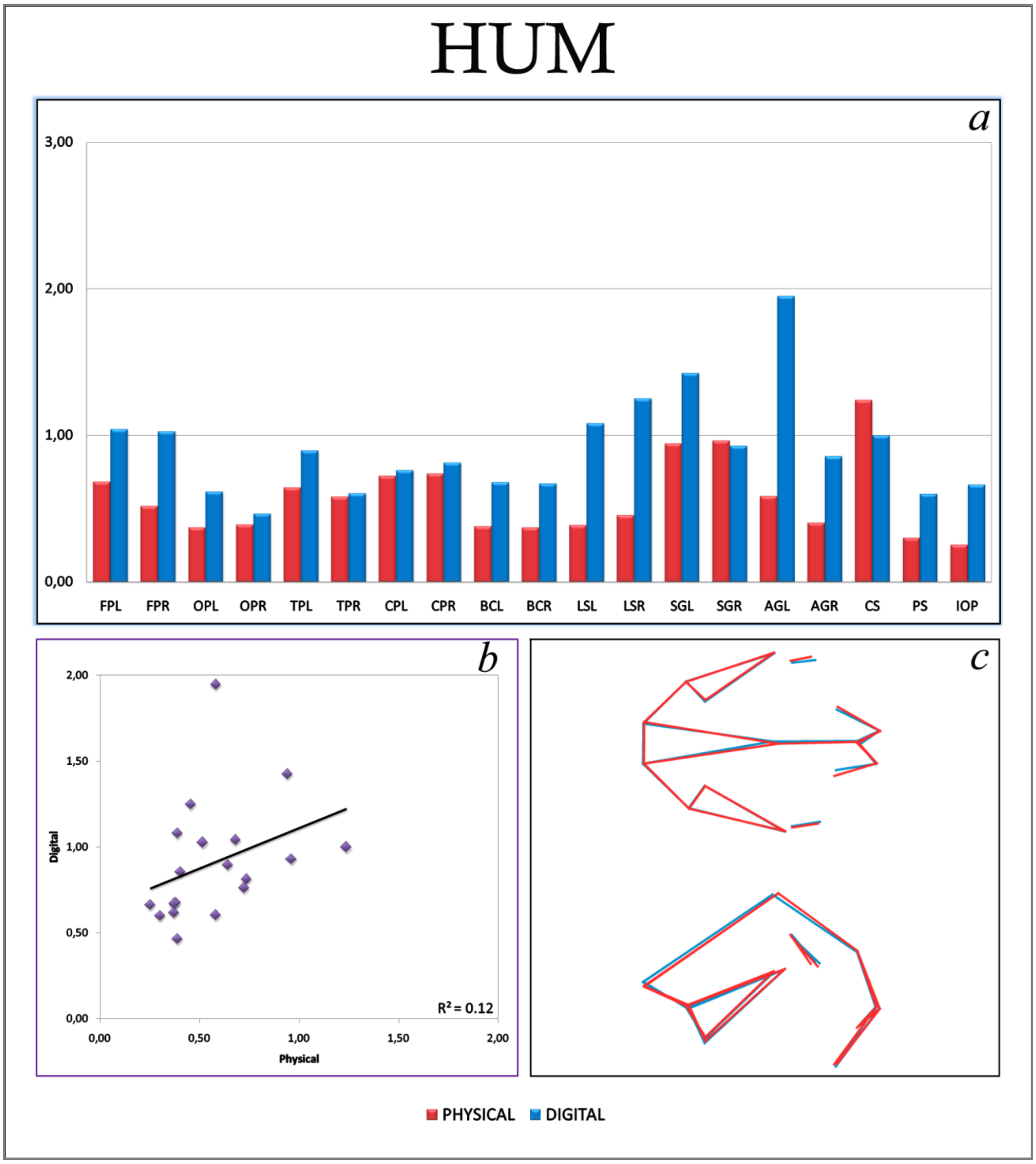

Figure 3.16. Differences between physical and digital variation on human. Charts compare (a) and correlate (b) error values per landmark. Wireframes illustrate the pairwise comparison between physical and digital mean shapes, showing the superior (above, left side up) and lateral (below) views.

Orangutan

On ORG, greater discrepancies between physical and digital values are exhibited by the right LS, SG and left AG, with larger error on the physical sample, and on right AG and PS, with larger error on the digital sample (figure 3.17a). SG displays larger error on the physical sample both on left (1.39) and right (1.55) sides, comparing to the digital (0.64 left; 0.57 right). AG displays the largest error value of the physical sample on the left side (1.65), and, on the right side, it displays the largest error value of the digital sample (1.72). The error on the right for the physical sample (1.37) and on the left on the digital sample (1.01) is large as well. Regarding the perpendicular sulcus, the error on the digital sample (0.97) doubles the error on the physical (0.47).

Physical and digital error values are not correlated (R^2=0.07; figure 3.17b). The landmarks which location displays greater discrepancy between physical and digital samples are LS, SG and AG (figure 3.17c).

Siamang

SIA's landmarks displaying greater discrepancies between physical and digital error values are the angular gyrus and the internal occipital protuberance (figure 3.18a). AG and SG also exhibit discrepancies between sides. AG exhibits the larger error of the physical sample on the right side (1.80), and a considerable smaller value on the left side (0.91). On the digital sample, AG error values display smaller difference between left (1.30) and right (1.19). SG, on the contrary, display larger error on the left, both on physical (1.29) and digital (1.35) samples, and a smaller error on the right, with little difference between physical (0.88) and digital (0.82). On IOP the error value is larger on digital (0.84) than on physical (0.55). LS displays the same discrepancies pattern as AG, but with the error being larger on physical on the left and on digital in the right.

The error values from physical and digital samples exhibit the largest correlation of all endocasts (R^2=0.59; figure 3.18b). The pairwise comparison shows that physical and digital mean shapes are very similar, with a visible asymmetry between sides (figure 3.18c).

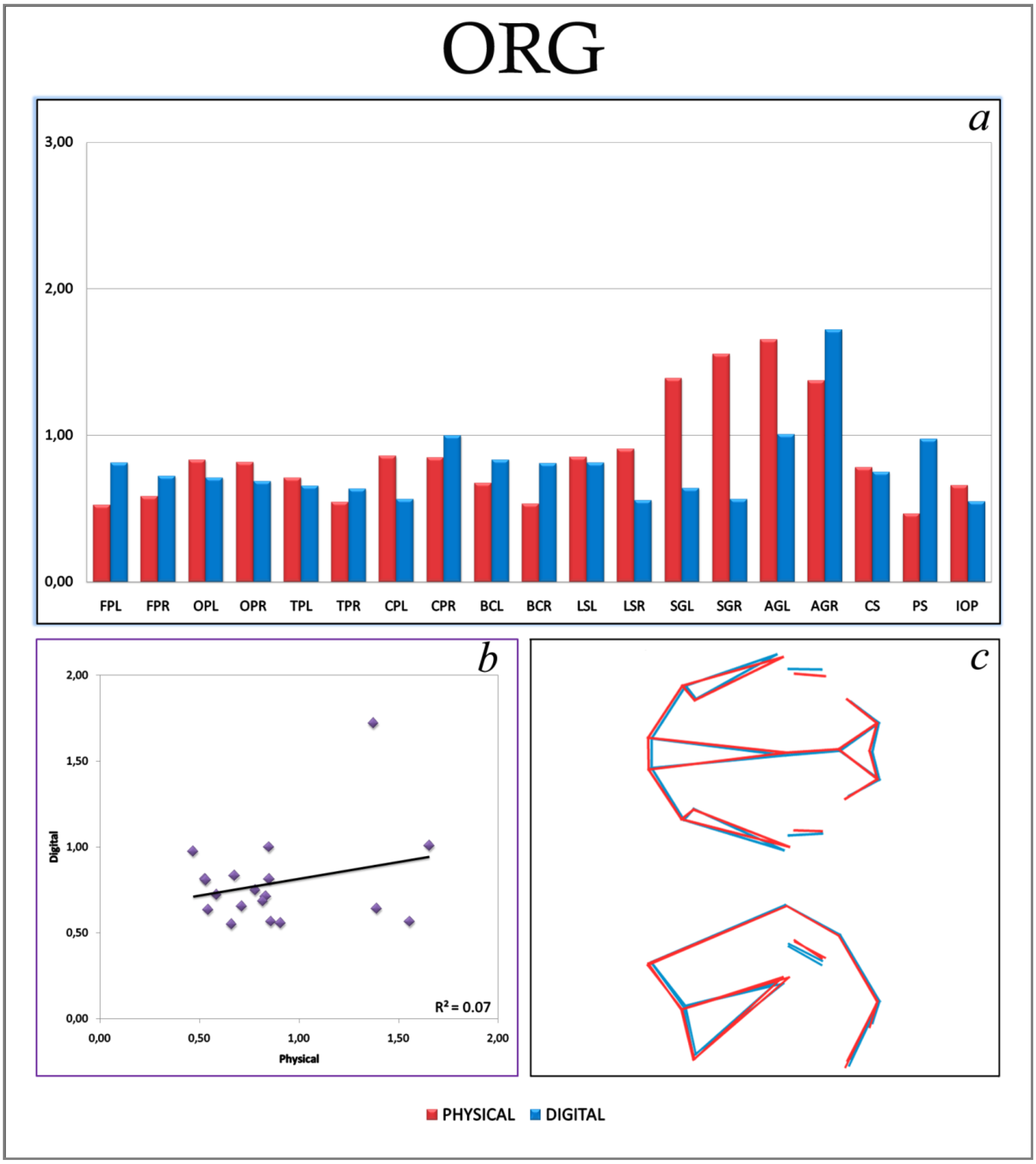

Figure 3.17. Differences between physical and digital variation on orangutan. Charts compare (a) and correlate (b) error values per landmark. Wireframes illustrate the pairwise comparison between physical and digital mean shapes, showing the superior (above, left side up) and lateral (below) views.

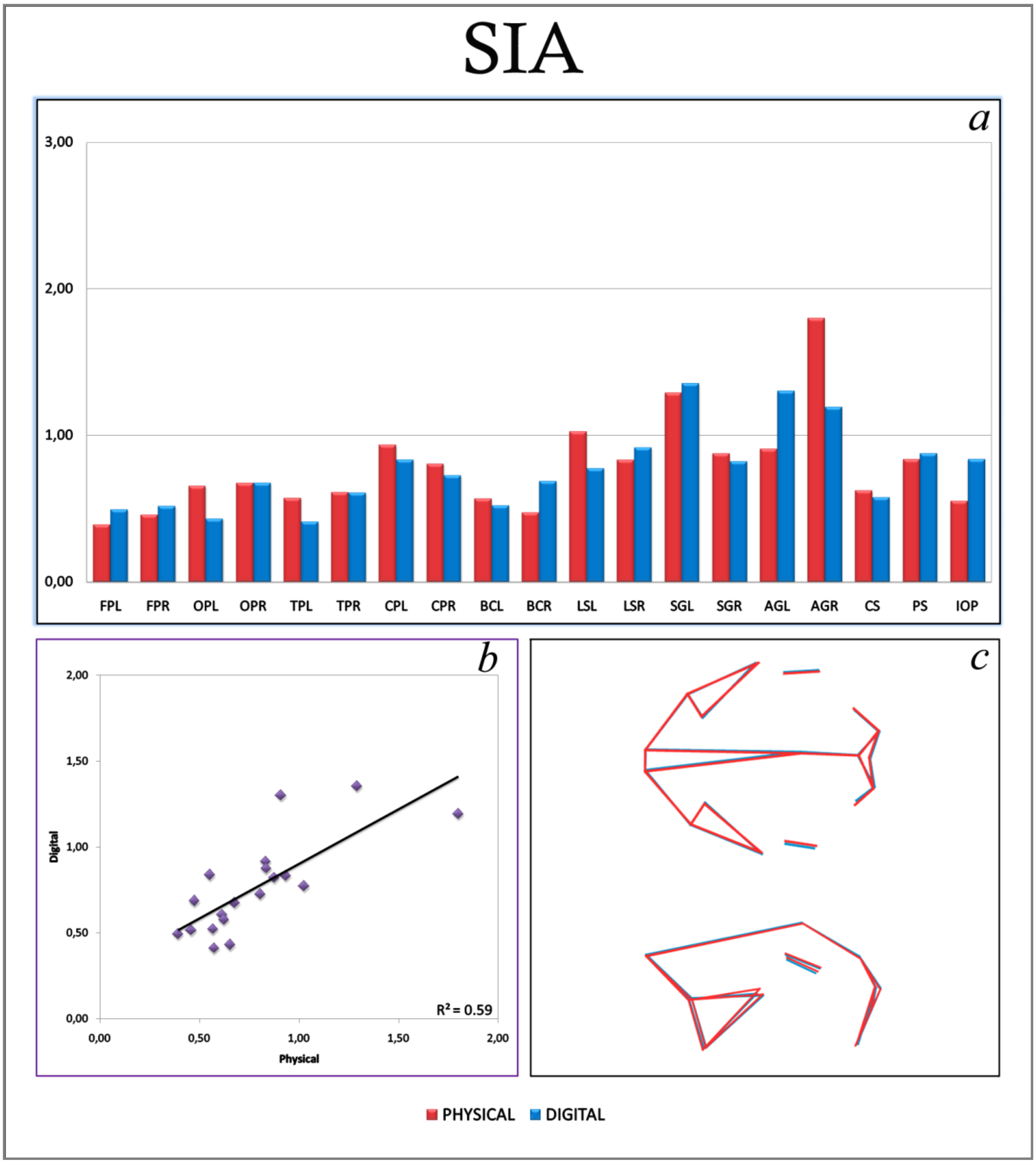

Figure 3.18. Differences between physical and digital variation on siamang. Charts compare (a) and correlate (b) error values per landmark. Wireframes illustrate the pairwise comparison between physical and digital mean shapes, showing the superior (above, left side up) and lateral (below) views.

3.2. SHAPE COMPARISON

PCA on figure 3.19 shows the specimens distribution in PC1-2 shape space according to their mean shapes. Along the first principal component shape changes mainly on the parietal area, with specimens that display lower scores having rounder endocasts with higher parietal area (LS, SG) and CS (taller brains), slightly lower frontal poles and Broca's cap and more anterior cerebellar poles. The second principal component separates shorter from longer brains. Specimens with lower scores display shapes with a higher and more posterior frontal poles, which are further apart from temporal poles and Broca's cap. In specimens having higher scores on PC2, CS and SG are on a more posterior position and LS is more anterior.

PC1 clearly separates HUM (lower scores) from the other apes (higher scores). The mean shapes of non human apes are also separated along PC1, from ORG with the lower score to SIA with the higher. CHIM and GIB have the closest scores on this PC, but note that, except for HUM, all the other specimens' scores overlap, when considering all the replicas (see figure 3.4). Along PC2, ORG displays the lower score and GIB the higher. In this PC BON and CHIF display scores that are closer to each other and to zero. GIB and GOR also display scores closer to each other.

When comparing the mean shapes of all male endocasts (figure 3.20) it is clear that HUM is the most markedly different. This difference is associated with PC1, with HUM having a rounder, taller and wider endocast. ORG also displays a rounder endocast, but shorter and narrower than that of HUM. BON seems to display the most average shape, as it is closer to zero on both principal components. Comparing to BON, CHIM has a thinner brain with higher frontal and occipital poles and lower supramarginal and angular gyri. CHIM and SIA seem very similar on the lateral view, with SIA having a lower parietal area. But the superior view shows that SIA's endocast is wider with more posterior Broca's cap. GIB and GOR wireframes exhibit the most similar shapes. Both have narrow and long brains with a high position of SG and AG. GIB is only a little wider than GOR, but still it is narrower and a little longer than SIA.

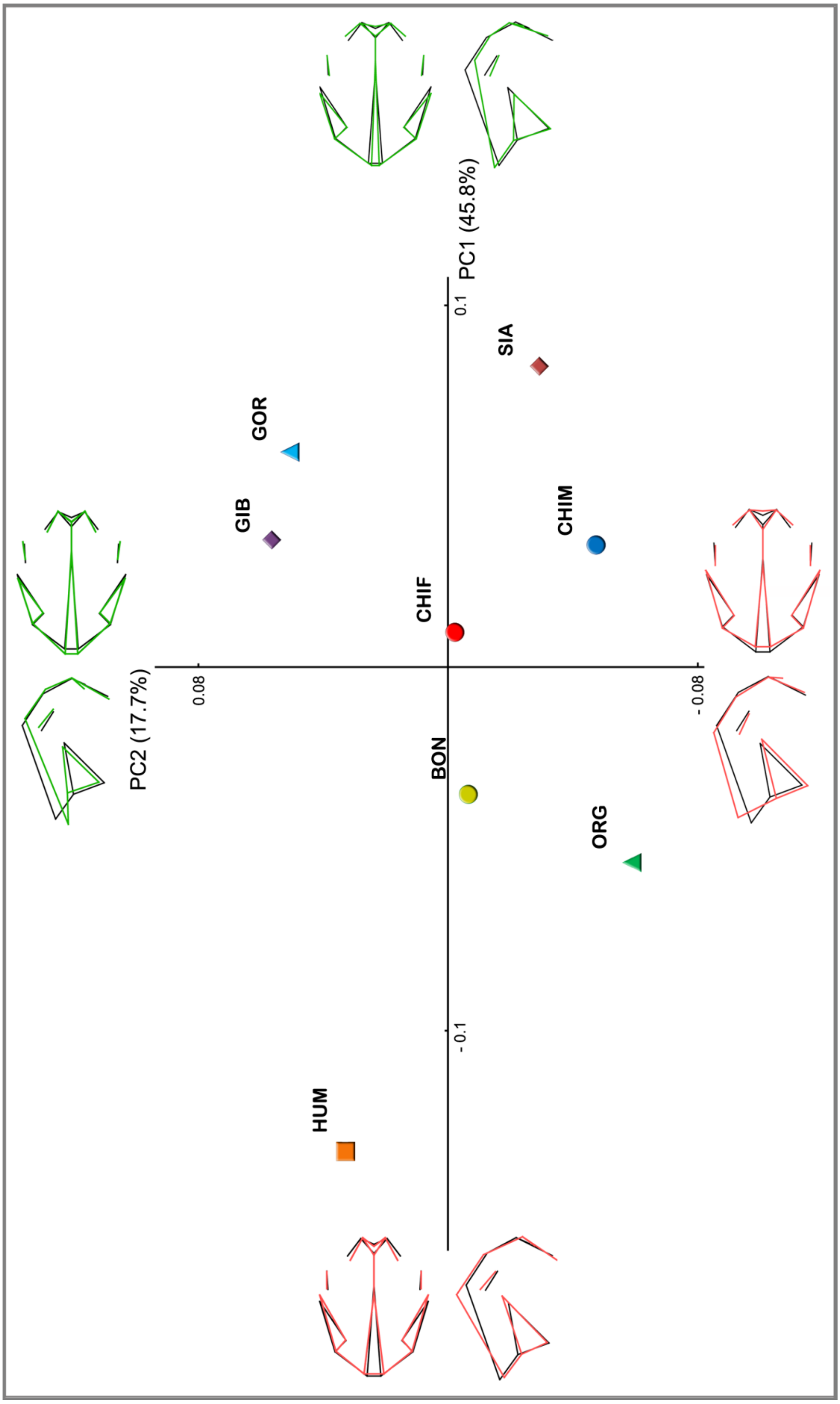

Figure 3.19. Distribution of each endocast mean shapes along PC1 (45.8% of variance) versus PC2 (17.7% of variance) shape space. Wireframes represent the shape extremes (red – negative scores; green – positive scores; black – central shape).

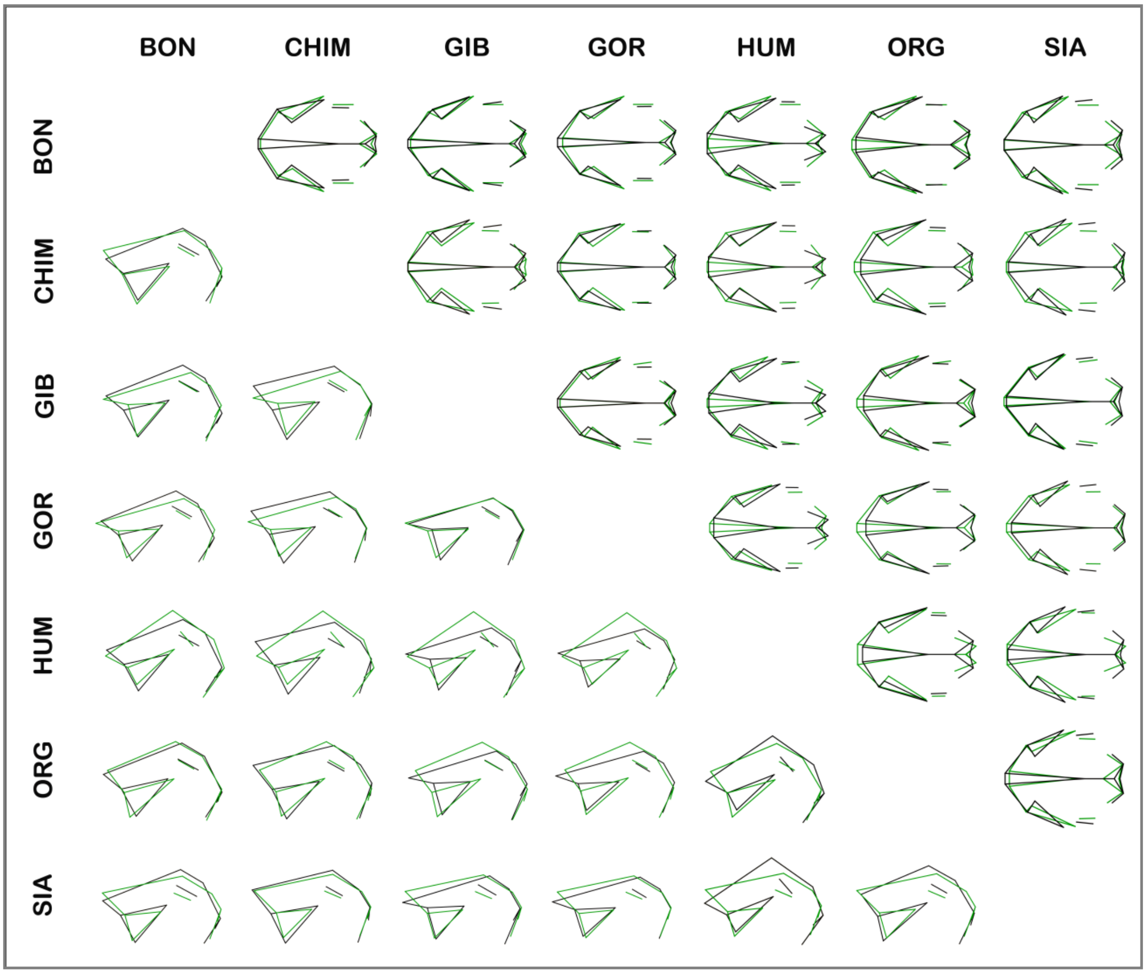

Figure 3.20. Comparison of mean shapes through pairwise Procrustes superimposition of wireframes for each endocast. Black wireframes correspond to specimens on the columns and green wireframes to those on the rows. Upper triangle: superior view, left side up; lower triangle: lateral view.

CHIM and CHIF are compared on figure 3.21 to assess differences related to gender. The male endocast is narrower and a little longer, with higher frontal and occipital poles, more anterior Broca's cap and lower temporal poles and angular gyrus. In fact, the anterior region of CHIF is overall vertically constricted, with the frontal poles closer to the temporal poles. Considering the parietal region, the major discrepancy is on the angular gyrus, which on CHIF is lower and closer to the lateral sulcus, and with larger distance between both angular gyri (left and right). In addition, CHIF's occipital poles also display larger distance between them, as well as to the cerebellar poles and to the internal occipital protuberance and perpendicular sulcus.

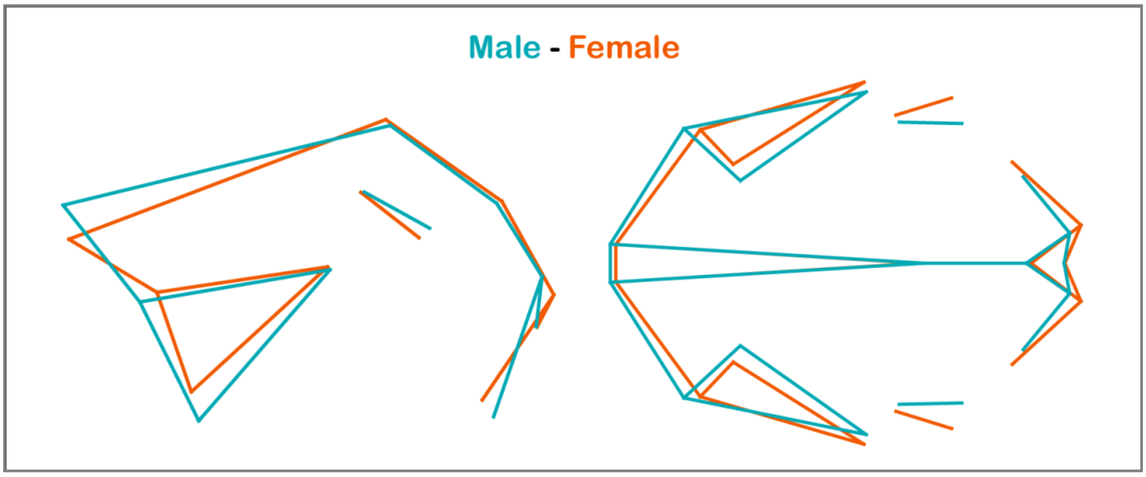

Figure 3.21. Comparison of mean shapes through pairwise Procrustes superimposition of chimpanzee female and male wireframes.

4. DISCUSSION

4.1. ERROR AND VARIATION

Absolute error

Most of the landmarks used in this analysis coincide with the landmarks used by Bruner (2010) in fossil endocasts, and which recognition he considered difficult and based on experience and subjectivity. Although the present study does not deal with fossils, some difficulties in localizing cortical brain structures on the endocranial casts were met as well. Even so, the absolute error in positioning landmarks seems to be relatively small. In fact, brain shape differences between genera and species can be easily assessed. Aldridge (2011) and Bienvenu *et* al. (2001) also calculated the error in locating landmarks. With the same procedure as the present study to calculate precision in locating brain landmarks, Aldridge (2011) obtained a mean error value of 1.97mm. Bienvenu and coworkers (2011) calculated the intra-observer error by subtracting the coordinates of a landmark by the coordinates of the same landmark collected on another sampling session of the same specimen. They obtained an average mean distance between landmarks of 1.37mm, which they considered low. The mean absolute error value resultant from the present work (0.86mm) is smaller than those of the cited works, thus the level of error of landmark repeatability is acceptable.

The largest uncertainty concerns the supramarginal gyrus, angular gyrus, and lateral sulcus. This is particularly true for the human endocast which, being the largest one has bigger and smoother areas. The lateral sulcus was also one of the landmarks with most error in the study by Bienvenu *et* al. (2011). But they found great mean distances on the four endocranial poles (frontal, occipital, temporal and cerebellar) and internal occipital protuberance as well. In the present work these landmarks displays the lower mean errors. This inconsistency is because Bienvenu *et* al. (2011) used a different set of landmarks, including both brain and cranial landmarks, with some type I landmarks that are easier to identify.

Physical *versus* Digital

Differences between physical and digital error patterns after Procrustes superimposition are noteworthy. The digital sample, containing the bulk of landmarks with larger error values, displays greater mean error as well as larger variation within PC1-4 shape space. However when considering the mean error landmark by landmark and specimen by specimen, some display larger error within the physical sample, and other within the digital sample. The larger error values on landmarks of the digital sample comparing to the same on the physical can be explained by the smoother surface of the laser scan endocasts and the impossibility to handle them, which difficult the placement of the landmarks. On the other hand, this explanation is in disagreement with those landmarks and specimens which display larger error values within the physical sample. The interpretation of these results should be aided by the analysis of the features and characteristics of each endocast.

Consider BON for example. During the record of landmarks coordinates on the physical endocast, the lateral sulcus was located, on the right side, on a little “depression” that was considered to mark the end point of the sulcus. But on the laser scan endocast this “depression” was larger, poorly defined, so there was more uncertainty in locating the landmark. On the left side, there is larger error because it lacked the “depression” helping to locate the end point of the lateral sulcus. Here, the error is larger on the physical sample than on the digital, what can be random once on both physical and digital the aid feature was absent. Regarding the supramarginal gyrus, the gyrus itself is difficult to define, and so is the position of the landmark. The location of the SG on the physical cast was aided by tactile features and color stains of the endocast, and considering symmetry of the bilateral landmarks. On the digital cast the features are less defined and more difficult to see, and the color pattern is associated with the relief/ topography and changes with the perspective. But the error is only larger on digital on the left SG; on the right side the error is slightly larger on the physical cast. On CHIM, lateral sulcus, supramarginal gyrus and central sulcus were all positioned in relation to blood vessels imprints that were easily seen on the physical cast, thus displaying larger error on the digital. CHIF and HUM, which also display larger error on the digital sample, are both clearly marked with blood vessels imprints that helped landmarks location.

With respect to landmarks displaying larger error in location on the physical endocasts, the angular gyrus of CHIM and CHIF are noteworthy. The greater discrepancy between physical and digital on AG of these specimens is due to an error of interpretation of the gyrus that resulted in the clustering of two groups of landmark configuration replicas on the PCA, mainly due to the different position of this landmark. Like the left SG of BON, other landmarks were located using color stains and tactile features as reference: GOR left lateral sulcus, HUM central sulcus, ORG supramarginal and left angular gyrus. But in these cases, it seems that instead of making the landmarks location easier, those features resulted in misleading. For example, on HUM, the presence of various blood vessels around the region of the central sulcus led to larger error as the landmark was probably not located in relation to the same specific vessel on all the sampling session of the physical endocast. Once these vessels were less defined on the digital cast the misleading was smaller or absent. Conversely, ORG, which displays poorly defined features, the difference between physical and digital casts in this term is not very marked. On GIB, as on ORG, there is little discrepancy between physical and digital error, except on the parietal landmarks. SIA also shows little discrepancy between physical and digital error, being the endocast exhibiting the larger correlation value. The difference between physical and digital error on these three endocasts seems to be random, related to the different types of visualization that lead to different strategies of landmark location.

In addition to the referred issues affecting landmarks location, the positioning of landmarks in relation to the position of others (e.g. below, anterior or posterior to) can also lead to some error when these relative positions are interpreted slightly differently. Examples of such landmarks are the SG and AG which were located in some extent with reference to the central sulcus, on BON; and the HUM's left AG, which error may be related to error on the left SG. A particularity of SIA that also influenced the location of some landmarks is the damaged region including the parietal area on the right side. This endocast displays a lack of continuity on the right higher parietal and frontal regions due to a damage on the original specimen. In consequence of this defect, SIA shows great asymmetry on that region. The locating of the parietal landmarks having into account the location of the same landmarks on the opposite side may also be cause of different error values among these landmarks, influenced by interpretation. In fact, the asymmetry inherent to the endocasts may explain the discrepancies between left and right on corresponding bilateral landmarks. Differences in the pattern of features displayed that can aid landmarks location leads to differences in the error values on left and right corresponding bilateral landmarks of the same endocast. For instance, GIB's lateral sulcus was located relatively to a vessel on the left side, a feature that was not visible on the right side.

Hence, various factors contribute to the discrepancy between physical and digital error patterns: the difficulty in identifying or defining the brain region (e.g. gyrus) where to locate one point (landmark), the possibility of dissimilar interpretation or perception of the brain region between two session samples, the influence of the features present or absent on each cast, the difference between physical and digital relatively to the features resolution. Post this, the main aspect influencing error patterns is the characteristics of each endocast. When features like blood vessels, brain bulges or sulcus, are well visible on the physical endocasts or on one of the sides and poorly defined or absent on the digital or on the other side, the interpretation is different, i. e. without features present that can be used to aid the location of landmarks, the positioning of those is done using a different approach (e.g. in relation to other landmarks). The different approaches lead to different error patterns of error that are linked to specific characteristics of each endocast. An idiosyncratic pattern of error is also mentioned by Schoenemann *et* al. (2006) concerning their comparison of digital and physical endocast reconstruction. Furthermore, the error of the observer, which is related to previous experience, and random error also influence the pattern of error. The fact that, of the physical casts, HUM is the one with overall smaller error can be because the human brain is an extensively studied organ. As an object of multidisciplinary studies, more information about the human brain can be found, particularly about its anatomy. Plus, the main cortical regions used in the present study were originally defined on a human brain. In comparison, studies on brains of non-human primates are more specific and less available. This makes it more difficult to identify the main brain regions on the non-human endocasts, and consequently the location of landmarks.

Despite the differences in the patterns of error, the physical and digital landmark configuration replicas of each endocast cluster together and the specimens are well separated, which means that these landmarks are reliable and can be used for inter-specific analyses. Even thought the digital sampling can bring larger variance than the physical, the divergence is not statistically significant and both methods lead to similar results. The major discrepancy was found on the parietal bosses, the supramarginal and angular gyrus.

4.2. SHAPE COMPARISON

Interspecific comparison

The analysis of shape within this work is purely complementary and no statistical inferences can be made as the sample is composed of only one specimen of each. Even so, the distribution of the specimens in the shape space is consistent with that obtained by Bienvenu *et* al. (2011). HUM is separated from the remaining specimens along PC1 due to the characteristically globular shape of the modern human brain. The globularity of the brain is caused by expansion of parietal, relative shortening of the occipital and frontal poles, and the rotation of the occipital and cerebellum forward and under the brain mass (Bruner, 2004). Among these data, the globularity of the human endocast is only clear in terms of vertical enlargement. HUM is the taller endocast, with a more anterior central sulcus and a higher and more posterior end of the lateral sulcus. HUM is also the wider specimen, but it is only notable in comparison to CHIM and GOR (figure 3.20), as on the study of Bienvenu *et* al. (2011). An important shape change related to globularity of the neurocranium, the flexion of the cranial base (Lieberman *et* al., 2002), is not comprised by the landmarks used in the present analysis.

Among the non-human apes, ORG is the specimen with the rounder shape, followed by BON. Displaying the higher scores, GIB, GOR, and specially SIA have more flatten endocasts, with lower central sulcus in relation to the frontal poles. On PC2, ORG displays the lower scores, being the shorter endocast, with higher frontal poles; and the higher scores are displayed by GOR and GIB, having longer brains, with the frontal poles closer to Broca´s cap. As in Bienvenu and colleagues' (2011) study, the Panins are closer to the consensus.

Aldridge (2011) also obtained clear separation between humans and the other apes, by using EDMA. She found significant differences on both internal and external parts of the brain, including the cortical surface, and frontal, parietal and temporal regions. Besides these differences between humans and all apes, each of the apes displays unique characteristics distinguishing them to humans. According to Aldridge (2011), chimpanzees have more anteroposterly expanded parietals and gorillas have more elongated non-frontal structures, relatively to humans. These results are in agreement with the more elongated brains of CHIM and especially GOR, found on the present study. Also in agreement with Aldridge's (2011) findings is the superoinferiorly elongated temporal of orangutans. The finding that the gibbon's occipital region is expanded mediolaterally comparing to humans (Aldridge, 2011) is corroborated by this study as GIB displays larger difference between the occipital poles. But Aldridge (2011) also found greater distance between the occipital poles on bonobos, which was not found here, as the distance between OP in HUM and BON are similar.

But Aldridge (2011) only compared the apes to humans, and not to each other, and Bienvenu *et* al. (2011) did not include the lesser apes on their analysis. The distribution of SIA and GIB on the present study is worth mentioning. The major differences between SIA and GIB are located on the frontal end parietal areas. SIA have lower parietal areas (SG and AG) and higher frontal poles that are further apart from Broca's cap. GIB is slightly longer and narrower (figure 3.20).

In fact, the morphology of GIB is more similar to that of GOR. The clustering of gorillas and gibbons was also documented by McNulty (2004), when studying hominoids cranial shape affinities. The author observed more affinity between hylobatids and gorillas than between any other pair of apes, especially after removing the variance associated with size. The author hypothesized a retention of cranial morphology by both *Gorilla* and *Hylobates* (McNulty, 2004), but Bienvenu *et* al. (2011) stated that gibbons and African apes do not share the same allometric trajectory, and considered that the determination of more primitive or derived endocranial morphologies need further study. In McNulty's (2004) analysis siamangs were included in the hylobatids, being the least similar to gorillas. The damage on the right parietal region of SIA may have influenced the differences between this specimen and GIB relatively the supramarginal and angular gyrus (PC1). Furthermor, *Hylobates* and *Symphalangus* differ in internal neurocranial and craniofacial angular relationships (Leslie, 2010). Leslie (2010) found siamangs to have more dorsally oriented orbits and significantly flatter skull base, relatively to gibbons. These differences in the ontogenic patterns of change in face orientation may be indicative of changes in brain organization between the two hylobatid genera. As these differences may not only be related to size, the inclusion of the lesser apes as a representative group into primate comparative studies can have significant implications (Leslie, 2010).

Chimpanzee sex dimorphism

Besides the distinct patterns that distinguish each non-human ape's from human's brains, Aldridge (2011) obtained as well differing sex-related patterns, i.e. females and males of each species differ from humans in distinctive characteristics. According to Bienvenu *et* al. (2001), among the great apes humans and gorillas display the greater sexual dimorphism in terms of endocranial volume, but only gorillas show significant dimorphism in endocranial shape. The sample used on the present study only allows sex comparison between the chimpanzee endocasts. Besides this comparison can be no more than preliminary and descriptive since just one specimen of each sex is available.

First, it should be noticed that the female chimpanzee is closer to the bonobo than to the male chimpanzee on the shape space (figure 3.19). Bonobo skull has been considered "paedomorphic" (juvenilized) in comparison to chimpanzee skull (e.g. Shea 1983; Mitteroecker *et* al., 2004; 2005; Lieberman *et* al., 2007), which is in agreement with bonobo being more similar to the female chimpanzee than to the male. Durrleman and colleagues (2012) confirm the developmental delay of bonobos relatively to chimpanzee in adulthood. Moreover, on their study bonobos endocrania differ from those of chimpanzee in being more globular at all stages. In the present analysis the rounder endocranial shape is a characteristic shared by the bonobo and the female chimpanzee endocasts that separates these from the male chimpanzee one. Thus, the present study is in agreement with all of the above.

In addition, the major differences between the endocasts of female and male chimpanzees were found on the fronto-temporal area and on the parietal region comprised by the angular gyrus. On their study of craniofacial sexual dimorphism in great apes, Schaefer *et* al. (2004) obtained significant differences between male and female in size and shape. Gorillas and orangutans are those with larger magnitude of sexual dimorphism on both size and shape, and chimpanzees cluster with humans and bonobos in terms of shape dimorphism (Schaefer *et* al., 2004). On chimpanzee the dimorphism is associated with non-allometric shape differences between male and female, which the authors suggest to be the sexual selection, as in humans (Schaefer *et* al., 2004). The differences in brain morphology of males and females among primates have been related to the social role of each gender inside their group (Lindenfors, 2005). Gur and colleagues (1999) associated the better performance on language tasks by women with the differences in intracranial tissue composition. Similarly, the different social demands of female and male chimpanzees (Lindenfors, 2005), may be associated to different morphology and shape of their brains.

5. CONCLUSIONS

Brain evolution is the field of Paleouneurology, which mainly relies on the analysis of endocasts. The analysis of shape can be accessed through the use of landmark data and multivariate statistics provided by GM. As the landmarks configuration influences the results, the precision and repeatability in landmark location is of great importance. Furthermore, the application of landmarks on endocasts is complicated by the difficulties in identifying the anatomical regions, which can be increased when dealing with digital endocasts.

The present study constitutes a preliminary analysis on a small sample of endocasts to evaluate intra-observer error in placing landmarks on major brain areas. Results suggest that cortical brain landmarks on endocasts show a good reliability for large scale taxonomic analysis. Although results are coherent between physical and digital data, in the latter case the lack of physical contact adds further difficulties in landmarking brain structures. The lower parietal bosses show the largest degree of discrepancy among the points considered in this analysis.

Regarding the shape comparison between the specimens, even though the extremely small size of the sample, the results fall within those obtained previously by other authors, strengthening the reliability of the chosen landmarks.

6. REFERENCES

Adams, D. C.; Rohlf, F. J.; Slice, D. E. 2004. Geometric morphometrics: ten years of progress following the 'revolution'. *Italian Journal of Zoology*, 71: 5-16.

Aldridge, K. 2010. Patterns of differences in brain morphology in humans as compared to extant apes. *Journal of Human Evolution*, 60 (2011): 64-95.

Baab, K. L.; McNulty, K. P.; Rohlf, F. J. 2012. The shape of human evolution: a geometric morphometric perspective. *Evolutionary Anthropology*, 21: 151-165.

Bienvenu, T.; Guy, F.; Coudyzer, W.; Gilissen, E.; Roualdès, G.; Vignaud, P.; Brunet, M. 2011.Assessing endocranial variations in great apes and humans using 3D data from virtual endocasts. *American Journal of Physical Anthropology*, 145(2):231-246.

Boddy, A. M.; McGowen, M. R.; Sherwood, C. C.; Grossman, L. I.; Goodman, M.; Wildman, D. E. 2012. Comparative analysis of encephalization in mammals reveals relaxed constraints on anthropoid primate and cetacean brain scaling. *Journal of Evolutionary Biology*, 25: 981-994.

Bookstein, F. L. 1991. *Morphometric tools for landmark data: geometry and biology.* Cambridge University Press: New York.

Bookstein, F. L. 1997. Shape and the information in medical images: a decade of the morphometric synthesis. *Computer Vision and Image Understanding*, 66(2): 97-118.

Bruner, E. 2003. Fossil traces of the human thought:paleoneurology and the evolution of the genus Homo. *Rivista di Antropologia:* 81, 29e56.

Bruner, E. 2004. Geometric morphometrics and paleoneurology: Brain shape evolution in the genus Homo. *Journal of Human Evolution*, 47: 279–303.

Bruner, E. 2007.Cranial shape and size variation in human evolution: structural and functional perspectives. *Child's Nervous System*, 23: 1357-1365.

Bruner, E. 2008. Comparing endocranial form and shape differences in modern humans and Neandertal: a geometric approach. *PaleoAnthropology*, 2008: 93-106.

Bruner, E.; Holloway, R. L. 2010. A bivariate approach to the widening of the frontal lobes in the genus *Homo*. *Journal of Human Evolution*, 58:138-146.

Bruner, E.; Jacobs, H. I. L. 2013. Alzheimer’s Disease: the downside of a highly evolved parietal lobe? *Journal of Alzheimer’s Disease*, 35:227–240.

Bruner, E.; Manzi, G.; Arsuaga, J. L. 2003. Encephalization and allometric trajectories in the genus Homo: Evidence from the Neandertal and modern lineages. *Proceedings of the National Academy of Sciences of the United States of America*, 100: 15335–15340.

Bruner, E.; Manzi, G. 2006. Digital tools for the preservation of the human fossil heritage: Ceprano, Saccopastore, and other case studies. *Human Evolution*, 21:33-44.

Bruner. E. 2010. Morphological differences in the parietal lobes within the human genus, a neurofunctional perspective. Current anthropology, 51:S77-S88.

Cramon-Taubadel, N.; Frazier, B. C.; Lahr, M. M. 2007. The problem of assessing landmark error in geometric morphometrics: theory, methods and modifications. *American Journal of Physical Anthropology* 134:24-35.

Deaner, R. O.; Isler, K.; Burkart, J; van Shaick, C. 2007. Overall brain size, and not encephalization quotient, best predicts cognitive abilities across non-human primates. *Brain, Behavior and Evolution*, 70: 115-124.

Di Ieva, A.; Bruner, E.; Davidson, J.; Pisano, P.; Haider, T.; Stone, S. S.; Cusimano, M. D.; Tschabitscher, M., Grizzi, F. 2013. Cranial sutures: a multidisciplinary review. *Childs Nervous System*, 29:893–905.

Durrleman, S.; Pennec, X; Trouvé, A.; Ayache, N.; Braga, J. 2012. Comparison of the endocranial ontogenies between chimpanzees and bonobos via temporal regression and spatiotemporal registration. *Journal of Human Evolution*, 62:74-88.

Falk, D. 2007. Evolution of the primate brain. *In* Henke, W.; Tattersall, I. (eds.), *Handbook of palaeoanthropology Vol. 2: Primate evolution and human origins*, p. 1133 – 1162. Heidelberg: Springer-Verlag.

Falk, D. 2012. Hominin Paleoneurology: where are we now? *In*: Hofman, M. A.; Falk, D. (eds). *Progress in Brain Research, Volume 195*: Evolution of the Primate Brain, From Neuron to Behavior, Elsevier p. 255-272.

Free, S. L.; O'Higgins, P.; Maudgil, D. D.; Dryden, I. L.; Lemieux, L.; Fish, D. R.; Shorvon, S. D. 2001. Landmark-based morphometrics of the normal adult brain using MRI. *NeuroImage*, 13: 801-813.

Friess, M. 2012. Scratching the surface? The use of surface scanning in physical and paleoanthropology. *Journal of Anthropological Sciences*, 90: 1-26.

Gabi, M.; Collins, C. E.; Wong, P.; Kaas, J. H.; Herculano-Houzel, S. (2010). Cellular scaling rules for the brain of an extended number of primate species. *Brain Behavior and Evolution,* 76: 32–44.

Gunz, P.; Mitteroecker, P.; Neubauer, S.; Weber, G. W.; Bookstein, F. L. 2009.Principles for the virtual reconstruction of hominin crania. *Journal of Human Evolution*, 57:48-62.

Gunz, P.; Neubauer, S.; Maureille, B.; Hublin, J. J. 2010. Brain development after birth differs between Neanderthals and modern humans. *Current Biology*, 20: R921-R922.

Gur, R. C.; Turetsky, B. I.; Matsui, M.; Yan, M.; Bilker, W.; Hughett, P.; Gur, R. E. 1999. Sex Differences in Brain Gray and White Matter in Healthy Young Adults: Correlations with Cognitive Performance. *The Journal of Neuroscience*, 19(10):4065–4072

Hammer, Ø.; Harper, D. A. T. 2006. *Paleontological data analysis*. Blackwell Publishing: Oxford.

Hammer, Ø.; Harper, D. A. T.; Ryan, P. D. 2001. PAST: Paleontological statistics software package for education and data analysis. *Palaentologia Electronica,* 4:1–9.

Herculano-Houzel, S. 2012. The remarkable, yet not extraordinary, human brain as a scaled-up primate brain and its associated cost. *Proceedings of the National Academy of Sciences of the United States of America,* 109: 10661-10668.

Holloway, R. L. 1975. *The role of human social behavior in the evolution of the brain (James Arthur lecture on the evolution of the human brain, no. 43, 1973).* American Museum of Natural History: New York.

Holloway, R. L.; Broadfield, D. C.; Yuan, M. S. 2004. *The Human Fossil Record, Volume 3: Brain Endocasts, The Paleoneurological Evidence*. Wiley-Liss, Hoboken

Klingenberg, C. P. 2010. Evolution and development of shape: integrating quantitative approaches. *Nature Reviews Genetics*, 11:623–635.

Klingenberg, C. P. 2011. MorphoJ: an integrated software package for geometric morphometrics. *Molecular Ecology Resources,* 11**:** 353-357.

Klingenberg, C. P. 2013. Visualizations in geometric morphometrics: how to read and how to make graphs showing shape changes. *Hystrix*, 24(1) [Online] DOI: 10.4404/hystrix-24.1-7691.

Leslie, E. R. 2010. A comparative analysis of internal cranial anatomy in the Hylobatidae. *American Journal of Physical Anthropology*, 143:250-265.

Lieberman, D. E.; Carlo, J.; Ponce de León, M.; Zollikofer, C. 2007. A geometric morphometric analysis of heterochrony in the cranium of chimpanzees and bonobos. *Journal of Human Evolution*, 52:647-662.

Lieberman, D. E.; McBratney, B. M.; Krovitz, G. 2002. The evolution and development of cranial form in *Homo sapiens*. *Proceedings of the National Academy of Sciences of the United States of America,* 99(3):1134-1139.

Lindenfors, P. 2005. Neocortex evolution in primates: the ‘social brain’ is for females. *Biology Letters*, 1, 407–410.

McNulty, K. P. 2004. A geometric morphometric assessment of hominoid crania: conservative African apes and their liberal implications. *Annals of Anatomy*,186:429-433.

Mitteroecker, P.; Gunz, P.; Bernhard, M.; Schaefer, K.; Bookstein, F. L. 2004. Comparison of cranial ontogenetic trajectories among great apes and humans. *Journal of Human Evolution*, 46:679-698.

Mitteroecker, P.; Gunz, P.; Bookstein, F. L. 2005. Heterochrony and geometric morphometrics: a comparison of cranial growth in Pan paniscus and Pan troglodytes. Evolution and Development, 7:244-258.

Moss, M. L.; Young, R. W. 1960.A functional approach to craniology. *American Journal of Physical Anthropology*, 18:281-292.

Neubauer, S.; Gunz, P.; Hublin, J. J. 2009. The pattern of endocranial ontogenetic shape changes in humans. *Journal of Anatomy*, 215: 240-255.

Neubauer, S.; Gunz, P.; Hublin, J. J. 2010. Endocranial shape changes during growth in chimpanzees and humans: A morphometric analysis of unique and shared aspects. *Journal of Human Evolution*, 59: 555–566.

Neubauer, S.; Gunz, P.; Weber, G. W.; Hublin, J. J. 2012. Endocranial volume of Australopithecus africanus:new CT-based estimates and the effect of missing data and small sample size. *Journal of Human Evolution*, 62(4):498-510.

Neubauer, S.;Hublin, J. J. 2012. The evolution of human brain development. *Evolutionary Biology*, 39(4): 568-586.

O' Higgins, P. 2000. The study of morphological variation in the hominid fossil record: biology, landmarks and geometry. *Journal of Anatomy*, 197:103-120.

Reader, S. M.; Laland, K. N. 2002 Social intelligence, innovation, and enhanced brain size in primates. *Proceedings of the National Academy of Sciences of the United States of America,* 99: 4436–4441.

Ribas, G. C.; Yasuda, A.; Ribas, E. C,; Nishikuni, K.; Rodrigues, A. J. Jr. 2006. Surgical anatomy of microneurosurgical sulcal key points. *Neurosurgery*, 59(4): ONS-177-ONS-211.

Richtsmeier, J. T.; Aldridge, K.; Valerie, B. D.; Panchal, J.; Kane, A. A.; Marsh, J. L.; Yan, P.; Cole III, T. M. 2006. Phenotypic Integration of Neurocranium and Brain. *Journal of Experimental Zoology Part B: Molecular and Developmental Evolution,* 306(4): 360–378.

Richtsmeier, J. T.; Deleon, V. B.; Lele, S. R. 2002. The promise of geometric morphometrics. *Yearbook of Physical Anthropology*, 45:63-91.

Richtsmeier, J. T.; Paik, C. H.; Elfert, P. C.; Cole, T. M.; Dahlman, H. R. 1995. Precision, repeatability, and validation of the localization of cranial landmarks using computed tomography scans. *Cleft Palate - Craniofacial Journal*, 32(3):217-227.

Rilling, J. K. 2006. Human and nonhuman primate brains: are they allometrically scaled versions of the same design? *Evolutionary Anthropology*, 15:65-77.

Rilling, J. K. 2008. Neuroscientific approaches and applications within anthropology. *Yearbook of Physical Anthropology*, 51: 2-32.

Rohlf, F. J. 1990. Morphometrics. *Annual Review of Ecology and Systematics*, 21:299-316.

Rohlf, F. J. 1998. On applications of geometric morphometrics to studies of ontogeny and phylogeny. *Systematic Biology*, 47(1):147-158.

Schaefer, K.; Mitteroecker, P.; Gunz, P.; Bernhard, M.; Bookstein, F. L. 2004. Craniofacial sexual dimorphism patterns and allometry among extant hominoids. *Annals of Anatomy*, 186:471-478.

Schoenemann, P. T.; Gee, J.; Avants, B.; Holloway, R. L.; Monge, J.; Lewis, J. 2007. Validation of plaster endocasts morphology through 3D CT image analysis.*American Journal of Physical Anthropology*, 132(2):183-92.

Seeley, R. R.; Stephens, T. D.; Tate, P. 2008. *Anatomy & Physiology*, Eighth Edition, McGraw-Hill, New York.

Semendeferi, K.; Teffer, K.; Buxhoeveden, D. P.; Park, M. S.; Bludau, S., Amunts, K; Travis, K.; Buckwalter, J. 2011. Spatial organization of neurons in the frontal pole sets humans apart from great apes. *Cerebral Cortex,*21:1485-1497.

Shea, B. T. 1983. Paedomorphosis and neoteny in the pygmy chimpanzee. *Science*, 222:521-522.

Shultz, S.; Dunbar, R. 2010. Encephalization is not a universal macroevolutionary phenomenon in mammals but is associated with sociality. *Proceedings of the National Academy of Sciences of the United States of America,* 107: 21582–21586.

Slice, D. E. 2007. Geometric morphometrics. *Annual Review of Anthropology*, 36: 261-281.

Spoor, F.; Jeffery, N.; Zonneveld, F. 2000. Using diagnositic radiology in human evolutionary studies. *Journal of Anatomy*, 197: 61-76.

Valeri, C. J.; Cole III, T. M.; Lele, S.; Richtsmeier, J. T. 1998. Capturing data from three-dimensional surfaces using fuzzy landmarks. *American Journal of Physical Anthropology*, 107:113-124.

Wiley, D. F.; Amenta, N.; Alcantara, D. A.; Ghosh, D.; Kil, Y. J.; Delson, E.; Harcourt-Smith, W.; Rohlf, F. J.; St. John, K.; Hamann, B. 2005. Evolutionary Morphing. In. *Proceedings of IEEE Visualization*, Conference Publications, 431 – 438.

Zelditch, M.L., Swidersky, D.L., Sheets, H.D., and Fink, W.L. 2004. *Geometric morphometrics for biologists*. Elsevier, San Diego.

Zollikofer, C. P. E.; Ponce de Leon, M. S. 2013. Pandora's Growing Box: Inferring the Evolution and Development of Hominin Brains from Endocasts. *Evolutionary Anthropology*, 22:20–33.

Zollikofer, C. P. E.; Ponce De León, M. S.; Martin, R. D. 1998. Computer-assisted paleoanthropology. *Evolutionary Anthropology*, 6 (2): 41–54.

APPENDICES

APPENDIX A

Absolute Error Raw Values

Table A1. Raw values of absolute error per landmark and per specimen for the digital sample.

Landmark		BON	CHIM	CHIF	GIB	GOR	HUM	ORG	SIA
Frontal Pole	**L**	0.71	0.22	0.29	0.22	0.69	1.92	1.19	0.22
	R	0.63	0.32	0.43	0.15	0.85	1.9	1.00	0.2
Occipital Pole	**L**	0.54	0.53	0.83	0.38	1.14	0.67	0.44	0.23
	R	1.04	0.51	1.03	0.24	1.11	0.45	0.45	0.48
Temporal Pole	**L**	0.8	0.41	0.66	0.27	0.59	1.12	0.6	0.28
	R	0.92	0.54	0.55	0.33	0.64	0.99	0.56	0.38
Cerebellar Pole	**L**	0.69	1.12	0.7	0.57	0.56	1.21	0.57	0.57
	R	0.62	1.21	0.87	0.49	0.72	1.26	1.02	0.51
Broca's Cap	**L**	0.74	0.62	0.72	0.39	0.8	0.86	0.73	0.28
	R	0.82	0.75	1.01	0.24	0.71	0.79	0.69	0.41
Lateral Sulcus	**L**	1.17	0.84	1.18	1.11	0.48	1.77	0.71	0.52
	R	1.02	1.26	2.1	0.95	2.16	2.16	0.57	0.67
Supramarginal Gyrus	**L**	1.95	1.34	1.33	0.85	1.3	2.67	0.75	1.02
	R	0.91	1.77	1.19	0.73	1.08	1.53	0.55	0.71
Angular Gyrus	**L**	1.06	1.01	1.66	0.55	1.36	3.44	1.14	1.01
	R	1.55	0.85	1.86	0.87	1.05	1.34	1.98	0.92
Central Sulcus		0.82	1.04	0.85	0.43	0.55	1.31	0.64	0.35
Perpendicular Sulcus		0.88	0.58	0.82	0.36	1.11	0.43	1.01	0.58
Protuberance		0.59	0.52	0.58	0.23	0.93	0.74	0.42	0.49

For bilateral landmarks: **L** – left; **R** – right.

APPENDIX B

Significant PCs

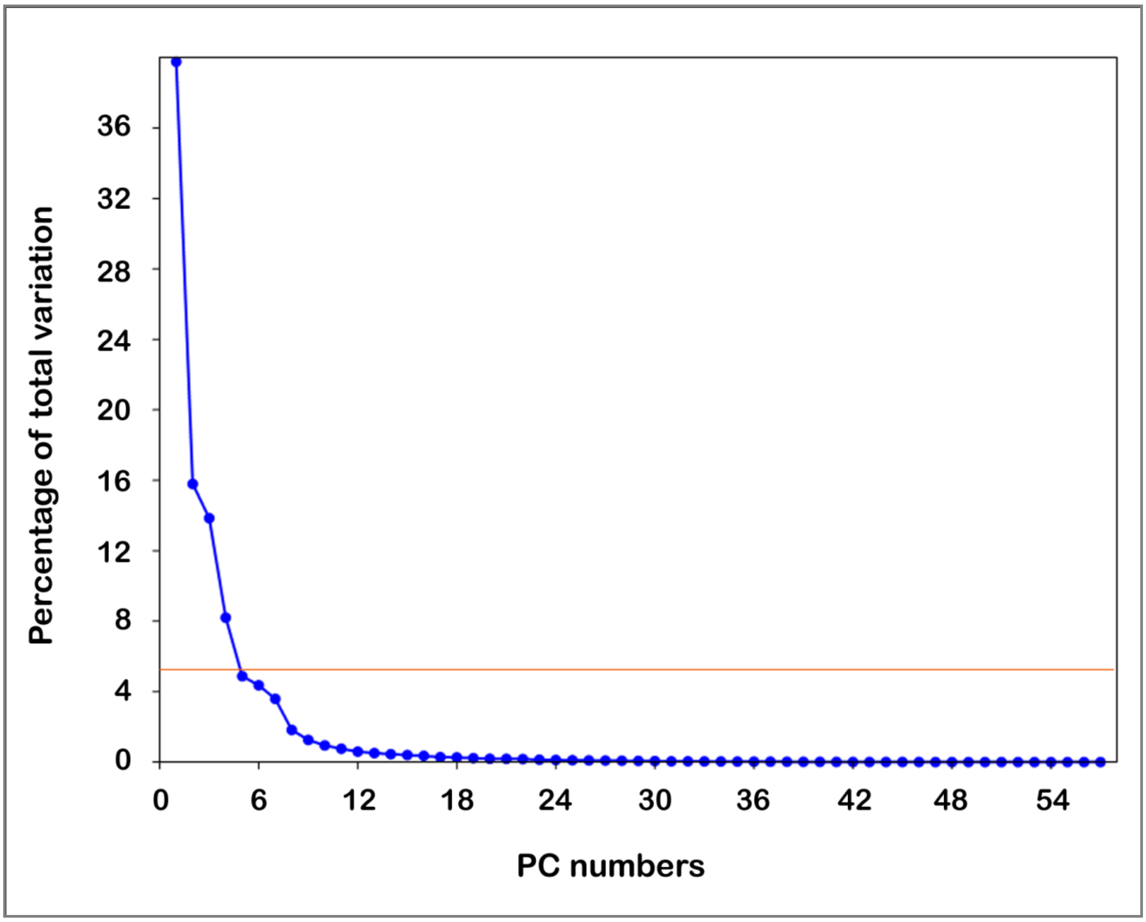

Figure B1. Scree plot. Significant PCs are PC 1-4 (variance > 5%).

Table B1. Eigenvalues and percentage of variance for the significant principal components (PC1-4).

PC	Eigenvalue	% variance
1	211.45	39.77
2	83.97	15.79
3	73.65	13.85
4	43.60	8.20

APPENDIX C

Error Values after Procrustes Superimposition

Table C1. Raw error values for the physical sample after Procrustes superimposition (physical + digital pooled).

Landmark		BON	CHIM	CHIF	GIB	GOR	HUM	ORG	SIA
Frontal Pole	**L**	0.65	0.39	0.42	0.48	0.34	0.68	0.53	0.39
	R	0.61	0.37	0.43	0.43	0.39	0.52	0.58	0.46
Occipital Pole	**L**	0.66	0.57	0.82	0.65	1.08	0.37	0.83	0.65
	R	1.03	0.41	0.72	0.63	1.12	0.39	0.82	0.68
Temporal Pole	**L**	0.83	0.79	0.63	0.57	0.56	0.64	0.71	0.57
	R	0.71	0.75	0.43	0.63	0.63	0.58	0.54	0.61
Cerebellar Pole	**L**	0.75	0.85	0.68	1.09	0.80	0.72	0.86	0.93
	R	0.65	0.86	0.71	0.96	0.63	0.74	0.85	0.80
Broca's Cap	**L**	0.97	0.79	0.51	0.82	0.47	0.38	0.68	0.57
	R	0.71	0.52	0.68	0.79	0.59	0.37	0.53	0.47
Lateral Sulcus	**L**	1.27	0.51	0.52	1.18	0.64	0.39	0.85	1.02
	R	0.50	0.76	0.52	1.68	1.40	0.46	0.91	0.83
Supramarginal Gyrus	**L**	0.65	0.65	0.85	0.79	1.16	0.94	1.39	1.29
	R	0.93	0.67	0.94	1.62	0.77	0.96	1.55	0.88
Angular Gyrus	**L**	1.03	3.01	2.48	1.67	1.69	0.58	1.65	0.91
	R	1.64	1.89	1.52	1.46	0.62	0.40	1.37	1.80
Central Sulcus		0.41	0.81	0.42	0.72	0.37	1.24	0.78	0.62
Perpendicular Sulcus		0.84	0.64	0.49	0.56	0.58	0.30	0.47	0.83
Protuberance		0.54	0.57	0.53	0.74	0.74	0.25	0.66	0.55

APPENDIX C

Error Values after Procrustes Superimposition

Table C2. Raw error values for the digital sample after Procrustes superimposition (physical + digital pooled).

Landmark		BON	CHIM	CHIF	GIB	GOR	HUM	ORG	SIA
Frontal Pole	**L**	0.70	0.41	0.61	0.39	0.66	1.04	0.81	0.49
	R	0.62	0.49	0.79	0.40	0.84	1.03	0.72	0.51
Occipital Pole	**L**	0.54	0.57	0.92	0.70	1.09	0.62	0.71	0.43
	R	1.05	0.58	1.02	0.51	1.20	0.46	0.69	0.67
Temporal Pole	**L**	0.83	0.52	0.78	0.48	0.59	0.90	0.65	0.41
	R	0.88	0.66	0.78	0.52	0.70	0.60	0.63	0.61
Cerebellar Pole	**L**	0.70	0.80	0.77	0.78	0.53	0.76	0.57	0.83
	R	0.62	0.86	1.04	0.75	0.85	0.81	1.00	0.72
Broca's Cap	**L**	0.80	0.54	0.84	0.67	0.75	0.68	0.83	0.52
	R	0.81	0.60	1.15	0.55	0.59	0.67	0.81	0.69
Lateral Sulcus	**L**	1.10	0.72	1.04	1.58	0.44	1.08	0.81	0.77
	R	0.92	1.06	1.76	1.39	1.88	1.25	0.56	0.91
Supramarginal Gyrus	**L**	1.59	1.18	1.10	1.18	1.15	1.43	0.64	1.35
	R	0.81	1.51	0.96	0.97	0.92	0.93	0.57	0.82
Angular Gyrus	**L**	0.96	0.88	1.45	0.78	1.08	1.95	1.01	1.30
	R	1.40	0.78	1.52	1.16	0.90	0.86	1.72	1.19
Central Sulcus		0.92	1.06	0.91	0.85	0.52	1.00	0.75	0.58
Perpendicular Sulcus		0.89	0.61	0.86	0.59	1.01	0.60	0.97	0.87
Protuberance		0.67	0.58	0.81	0.50	0.84	0.66	0.55	0.84